Influence of Carbonate Solvents on Solid Electrolyte Interphase Composition over Si Electrodes Monitored by In Situ and Ex Situ Spectroscopies

Zhan-Yu Wu, Yan-Qiu Lu, Jun-Tao Li, Sandrine Zanna, Antoine Seyeux, Ling Huang, Shi-Gang Sun, Philippe Marcus, Jolanta Światowska

Influence of carbonate solvents on SEI composition over Si electrode monitored by *in situ* and *ex situ* spectroscopies

Zhan-Yu Wu[1], Yan-Qiu Lu[2], Jun-Tao Li[2]*, Sandrine Zanna[1], Antoine Seyeux[1], Ling Huang[3], Shi-Gang Sun[2,3], Philippe Marcus[1], Jolanta Światowska[1]*

[1] *PSL Research University, CNRS – Chimie ParisTech, Institut de Recherche de Chimie Paris (IRCP), 11 rue Pierre et Marie Curie, 75005 Paris, France*

[2] *College of Energy, Xiamen University, Xiamen 361005, China*

[3] *State Key Laboratory of Physical Chemistry of Solid Surfaces, College of Chemistry and Chemical Engineering, Xiamen University, Xiamen 361005, China*

Abstract

SEI layer on Si-based anodes should have high mechanical properties to adapt the volume changes of Si, with low thickness and good ionic conductivity. To better understand the influence of carbonate solvents on SEI composition and mechanism of formation, systematic studies were performed using dimethyl carbonate (DMC) and propylene carbonate (PC) in $LiPF_6$ based electrolyte. 1 M $LiPF_6$/EC-DMC was used for comparison. The surface chemical composition of Si electrode was analyzed at different potentials of lithiation/delithiation and after a few cycles. *Ex situ* X-ray photoelectron spectroscopy and time-of-flight secondary ion mass spectrometry results demonstrate that a thinner and more stable SEI layer is formed in $LiPF_6$/DMC. The *in situ* Fourier transform infrared spectroscopy proves that the coordination between Li^+ and DMC is weaker and fewer DMC molecules take part in the formation of SEI layer. The higher capacity retention during 60 cycles and less significant morphological modifications of Si electrode in 1 M $LiPF_6$/DMC compared to other electrolytes were demonstrated, confirming a good and stable interfacial layer. The possible surface reactions are discussed and the difference in the mechanisms of formation of SEI in these three various electrolytes is proposed.

Keywords: Si thin film electrode; SEI layer; XPS; *in situ* FTIRS; ToF-SIMS; carbonate electrolyte

Corresponding authors: Jun-Tao Li, email: jtli@xmu.edu.cn, and Jolanta Światowska, email: jolanta.swiatowska@chimieparistech.psl.eu

1. Introduction

Silicon is one of the most promising candidates for the next generation of negative electrodes for Li-ion batteries due to its remarkably high specific capacity (reaching 3579 mAh g^{-1} at room temperature which corresponds to the formation of $Li_{3.75}Si$ alloy), high safety and low cost.[1–5] However, the cycle stability of Si anode is still limited by the huge volume expansion of Si (around 280% upon lithiation) resulting from the high ratio of Li in Li-Si alloy.[6–9] The volume expansion causes material pulverization,[10] electrical contact loss and poor cycle performance.[11–13] Moreover, the volume expansion/contraction during each cycle of lithiation/delithiation process also damages the solid electrolyte interphase (SEI) layer formed on the surface of Si electrode.[14] Thus, the SEI layer has to reconstruct on an uneven electrode surface and consumes an extra amount of lithium and electrolyte components during every cycle, which leads to irreversible capacity.[3,15] The irreversible capacity observed during the first lithiation can be as high as 30 %.[12] The composition of the SEI depends on the electrode material,[16] the nature of electrolyte (salt, solvent, additive)[17,18] and the conditions of lithiation/delithiation [11]. The SEI is formed by the electrochemical reduction of electrolyte at low potentials (close to 0.5 V).[11] The properties of the SEI can significantly influence the reversible capacity (columbic efficiency and energy efficiency) and battery cycle life.[16,19] Therefore, understanding the SEI formation mechanism and interfacial properties are considered as one of the key parameters for Li-ion battery design. The formation and composition of SEI have been widely studied on graphite electrode materials but much less on Si-based electrode materials. For commercial graphite anode, ethylene carbonate (EC) is an indispensable electrolyte co-solvent because it plays a key role in the formation of passive layer on the graphite surface to protect the graphite from Li-solvent co-intercalation, graphite exfoliation and continuous decomposition of electrolyte.[20] Thus, the other carbonate solvents such as DMC, PC and diethyl carbonate (DEC) cannot be applied without EC for graphite anode.[20,21] However, they could be used as the electrolyte solvents alone for Si anode, because Si is not a layered structure. The

electrolyte for Si anode is required to form the SEI layer that has better mechanical properties to adapt the volume changes and has lower thickness allowing better electrode conductivity.[19] Therefore, different kinds of electrolytes were employed on the Si-based anodes. Ohara *et al.* applied two different electrolytes 1 M $LiClO_4$/PC and 1 M $LiClO_4$/EC-DMC (1:1) on Si film electrodes. The electrodes in both electrolytes exhibit long stable cycle life.[22] Schroder *et al.* applied the 1 M $LiPF_6$/EC DEC (1:1) electrolyte on Si wafer electrodes and tested the cells by linear sweep voltammetry (LSV), cyclic voltammetry (CV) and chronoamperometry (CA) methods. X-ray photoelectron spectroscopy (XPS) data showed that the ratios of different species in the SEI layers became quite different after these electrochemical treatments.[23] Our research group employed previously 1 M $LiClO_4$/PC and 1 M $LiPF_6$/EC-DMC electrolytes on a-Si:H and Si nanowire electrodes and analyzed the SEI layers by XPS and time-of-flight secondary ion mass spectrometry (ToF-SIMS).[24] These studies allowed to conclude that the SEI layer formed in the PC-based electrolytes was thicker and richer in alkyl carbonate species, than that formed in EC:DMC-based electrolytes, which was mainly composed of salt decomposition products (LiCl or LiF).

In order to improve the Si-based electrode performances and the SEI properties on these electrodes, some electrolyte additives were also widely investigated for Si-based electrode materials such as vinylene carbonate (VC)[25–31] and fluoroethylene carbonate (FEC)[32–42]. These additives have some advantages of decomposition potentials higher than the main electrolyte solvents. However, the addition of the VC leads to higher cell impedance due to formation of the thicker SEI layer.[43] The FEC in electrolyte results in gas evolution at high temperatures, fast FEC consumption and finally a cell failure.[34] Therefore, the understanding of the reaction mechanisms of each single electrolyte component, the formulation of new electrolytes as well as a good approach in terms of analytical methods and fundamental studies of surface chemistry are necessary to optimize the performance of Si electrode.

The efficient approach in the chemical and structural characterization of the SEI layer is very important but not straightforward. For example, a lot of information

about the organic species on the SEI layer could be obtained by Fourier transform infrared spectroscopy (FTIRS) method. [44,45] *In situ* FTIRS was already applied for SEI studies on Si electrode.[41,46–49] Another powerful technique in characterization of the surface chemistry of electrode materials (organic and inorganic species) is XPS.[15,24,45,50–54] However, XPS has also different limitations: it is an ultrahigh vacuum *ex situ* technique, i.e. the sample needs to be rinsed and dried before analysis, which can lead to some surface modifications. Moreover, some of the peaks corresponding to different species can overlap (e.g. the Si-O or Si-F bonds in the region of Si 2p core level like demonstrated hereafter). ToF-SIMS, an extremely surface sensitive analytical method, can be used to analyze both surface and bulk electrode modifications (by means of ion in-depth profiling).[24,33,55,56] However, ToF-SIMS as a technique under vacuum has similar limitations as XPS.

The *ex situ* techniques such as scanning electron microscopy (SEM) and atomic force microscopy (AFM) are common techniques to observe the surface morphology of the electrode and the SEI layer.[16,57,58] As the surface topography might be changed after solvent washing and the sample exposition to the ambient air, several *in situ* techniques such as *in situ* electrochemical-AFM (EC-AFM) and *in situ* scanning transmission electron microscopy (STEM) can be applied to follow the surface modifications induced by lithiation/delithiation processes.[59–62] It should be noticed that to have a good insight into the formation of the SEI layer, the combination of different *ex situ* and *in situ* methods is necessary. Moreover, the good choice and simplified electrode materials (e.g. without binders) to avoid the ambiguities in the surface chemical and morphological characterization and to better understand the influence of the intrinsic properties of electrode materials on the SEI layer formation.

In this work, the systematic studies of surface characterization of Si thin film electrode in three electrolytes (1 M $LiPF_6$/EC-DMC, 1 M $LiPF_6$/DMC and 1 M $LiPF_6$/PC) were performed in order to better understand the influence of solvent on the SEI layer composition. Application of model thin film electrode allowed to avoid interference from other electrode components and additives such as binder and to determine more easily the different surface reaction mechanisms. It should be noticed

that the surface modifications of commercial composite Si-based electrodes can vary slightly. The analyses of the Si thin film were performed at different lithiation and delithiation potentials and after several cycles (5 cycles) by XPS, *in situ* microscope FTIRS and ToF-SIMS. The morphology of the Si thin film electrode was also examined by SEM. The capacity and columbic efficiency induced by cycling of Si thin film electrode were also tested as a function of electrolyte composition.

2. Results and discussion

2.1 Influence of lithiation/delithiation on the surface modifications of Si by XPS

2.1.1 Cyclic voltammetry of Si thin film electrode

The first cycle (CV curves) performed on Si thin film electrodes in different electrolytes (1 M $LiPF_6$/EC-DMC, 1 M $LiPF_6$/DMC and 1 M $LiPF_6$/PC) is shown in Figure 1. The two broad cathodic peaks particularly visible for EC-DMC electrolyte between 0.3 V and 2.0 V (also shown in the inset of Figure 1) correspond principally to the decomposition of electrolyte and the formation of SEI layer [63]. The peak corresponding to the electrolyte decomposition on the Si-based electrodes is the peak observed frequently at around 0.75 V.[11,24,41,49,64] Here for EC-DMC electrolyte, this peak is observed between C1 and C2 point. A reduction of small quantity of surface contaminations and/or traces of water occurring at higher potentials of around 1.5-1.0 V cannot be completely ruled out.[24,41] The most intense, narrow cathodic peaks between 0.01 V and 0.4 V correspond to the formation of Li-Si amorphous phases (Li_xSi),[65–67] whereas the high intensity two anodic peaks between 0.1 and 0.6 V corresponds to the phase transfer from Li-Si alloy to amorphous Si.[10,68–71] It should be noted that CV curves does not show a significant influence of electrolyte on their shapes. To demonstrate the differences in the surface composition of Si electrode cycled in these three different electrolytes, six points of lithiation (cathodic, C1-C4) and delithiation (anodic, A1 to A2) were chosen for XPS analysis:

- point C1 (~0.9 V) corresponding to the state after electrolyte decomposition and SEI formation and point C2 (~0.25 V) to the state before

lithiation,

- points C3 (~0.08 V) and C4 (~0.01 V) corresponding to the state after the first and the second lithation peak,
- point A1 (at ~0.015 V) corresponding to the beginning of delithiation process and point A2 (~1.0 V) to the end of delithiation process.

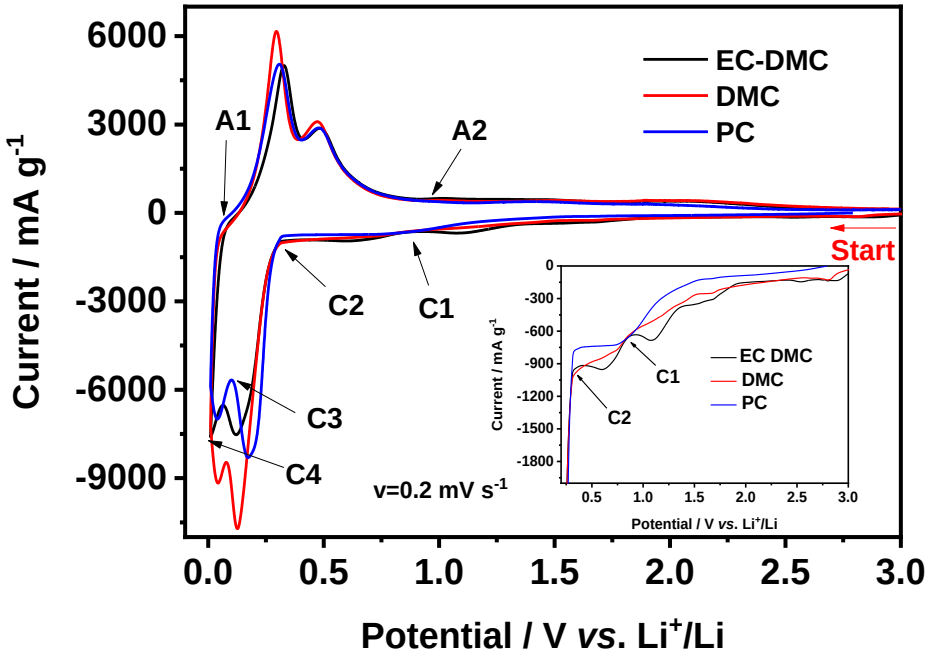

Figure 1 First CV cycle for Si thin film electrodes performed in different electrolytes: 1 M $LiPF_6$/EC-DMC, 1 M $LiPF_6$/DMC or 1 M $LiPF_6$/PC (scan rate v = 0.02 mV s^{-1}).

.

2.1.2 SEI layer formation in DMC-based electrolyte

The high resolution XPS spectra of Si 2p, C 1s, F 1s and O 1s for pristine Si electrodes and for the Si electrode after formation of SEI layer (point C2) and before delithiation (point A1) and after delithiation (point A2) in 1 M $LiPF_6$/DMC electrolyte are shown in Figure 2. For clarity of presentation, the detailed decomposition was only presented here for selected stages of lithiation/delithiation of Si in 1 M $LiPF_6$/DMC. The XPS decompositions (C 1s, F 1s and O 1s peaks) for all electrolytes and at all stages of lithiation/delithiation (points C1 to C4 and A1, A2) are presented

in the supplementary information (Figure S2, S3 and S4). All carbon, oxygen, fluorine and silicon characteristic species, their binding energies (BE) and full width at half maximum (FWHM) used in the peak decomposition are presented in Table 1.

In Figure 2, the Si 2p spectrum displays Si $2p_{3/2}$ and Si $2p_{1/2}$ spin orbit doublet. A theoretical value (1:2) of area ratio of Si $2p_{1/2}$:Si $2p_{3/2}$ peak was fixed for decomposition. The decomposition of Si 2p core level peak shows that the surface of the pristine Si thin film electrode prepared by magnetron sputtering is covered by a thin native Si oxide layer. The lowest binding energy peak at ~99.1 eV (Si $2p_{3/2}$) can be attributed to Si^0 [64,72] and three higher binding energy peaks (Si $2p_{3/2}$) to different Si oxides (Si^+ at ~100.2 eV, Si^{2+} at ~101.8 eV and Si^{4+} at ~103.5 eV, Table 1).[69,72–75] After the lithiation (C2) and delithiation (A1 and A2), the SEI layer was formed on the surface of Si thin film. The intensity of Si signal decrease significantly, but it could still be detected from the electrode bulk, probably due to the fractures, pores in the SEI layer or its not homogenous formation. After correction of binding energy versus carbon peak (C-C at 285.0 eV), the Si 2p peaks shift to lower binding energies because of the differential charging effects on different compounds formed on the surface of Si electrode.[24,69] Therefore, after electrochemical processes these Si 2p peaks were assigned to different Si compounds by calculating the difference in the binding energies corresponding to Si^0 and other Si peaks ($\Delta BE = BE_{Si0} - BE_{Si2+ \text{ or } 4+}$ as shown in Table 1). Then, the Si $2p_{3/2}$ peak at ~97.8 eV was assigned to Si^0, a peak at ~100.8 eV to Si^{2+} (Si-O, Si-F or $LiSi_xO_y$).[69,73,74,76] The Si $2p_{3/2}$ peak at ~102.9 eV could be assigned to Si^{4+} oxide and fluoride.[73,76] The peak at ~104.7 eV corresponds to SiO_xF_y.[72,73,77]

The C 1s profile (Fig.2) shows a large C-H, C-C peak (~285.0 eV) and small peaks corresponding to the $-OCH_3$ (~287.1 eV) and O-C=O (~288.9 eV) contaminations on pristine Si sample.[3,4,24,78,79] After the electrolyte decomposition and SEI formation processes (point C2), the $-OCH_3$ peak becomes very intense principally due to the electrochemical reduction of DMC solvent according to reaction (3) shown in scheme 1.[20,41,80] A small amount of $-CH_2OCO_2-$, Li_2CO_3 (~290.0 eV) can be also observed.[3,4,11,24,79,81,82] The most probably principal component here is Li_2CO_3 due to

the decomposition of DMC according to reaction (5). The relative intensities of O-C=O and -CH_2OCO_2-, Li_2CO_3 peaks becomes much higher after lithiation (at point A1). This phenomenon could be related to the changes of SEI layer composition during the lithiation process. After delithiation (at point A2), the -CH_2OCO_2-, Li_2CO_3 peak disappears and the intensity of O-C=O peak decreases, while the intensity of peak -OCH_3 peak increase. It probably indicates that the -CH_2OCO_2- and Li_2CO_3 species decomposed or some new C-H, C-C and -OCH_3 species formed and covered the surface during the delithiation process on the Si electrode in 1 M $LiPF_6$/DMC electrolyte.

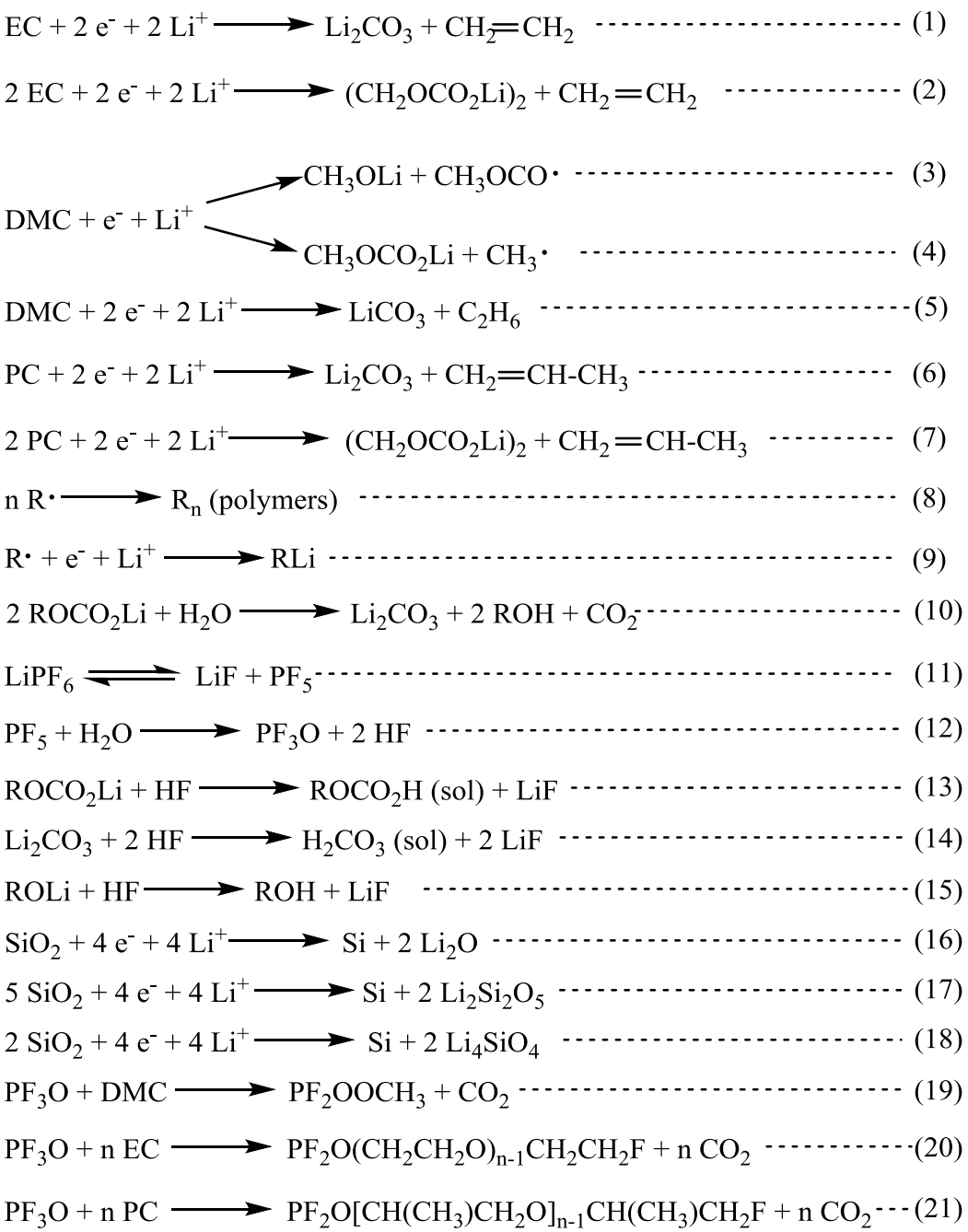

Scheme 1. Reduction reactions on Si thin film electrode with different electrolytes (1 M $LiPF_6$/EC-DMC, 1 M $LiPF_6$/DMC and 1 M $LiPF_6$/PC).

There is no F on the pristine Si sample. However, the high intensity of F 1s peak appears already after the first stage of lithiation (point C2). This peak can be decomposed in three components: Li-F (at ~685.1 eV),[3,4,11,24,79,82] SiOF (at ~686.8 eV)[73,74,76,83] and P-F (at ~688.1 eV)[3,4,24,79,82] as shown in Table 1. A very high intensity of SiOF component (e.g. SiO_xF_y) at different stages of lithiation/delithiation illustrates that the SEI layer formed on the Si electrode in 1 M $LiPF_6$/DMC samples is not very thick. The P-F signal (at ~688.1 eV) keeps at a relatively low intensity during the whole cycle and the Li-F signal (~685.1 eV) increases during the lithiation process and decreases during the delithiation process, demonstrating a formation and decomposition of LiF salt according to reactions (11)-(15).[31,41,84,85]

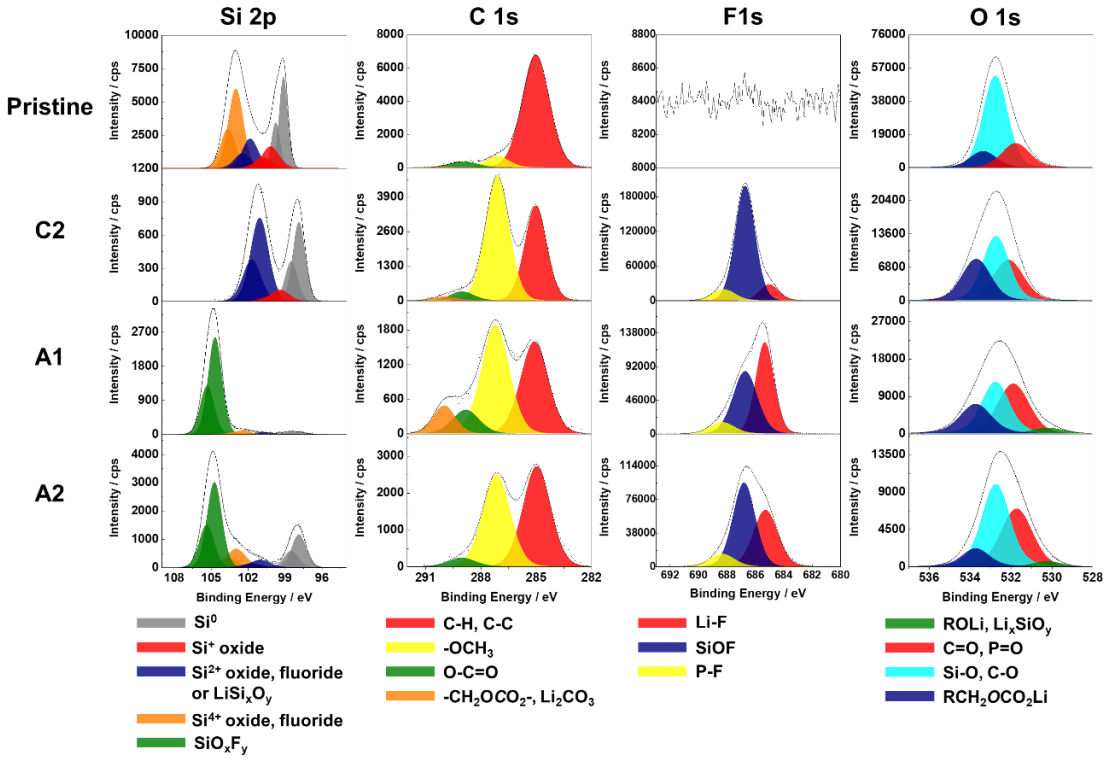

Figure 2 High resolution Si 2p, C 1s, F 1s and O 1s core level spectra obtained on the pristine surface of Si thin film electrode and on Si thin film after different stages of lithiation/delithiation (points C2, A1 and A2) in 1 M $LiPF_6$/DMC.

The O 1s profile for pristine Si sample shows as a major component the peak at ~532.9 eV corresponding to Si-O bonding, which is in agreement of Si 2p core level peak where the presence of SiO_x is observed.[3,4,24,81,82] The other two peaks at around 533.6 eV and 531.8 eV correspond to -CH_2*O*CO_2- and C=O surface organic compounds and/or organic surface contaminations, respectively (Table 1). After electrolyte decomposition and SEI formation processes (point C2), RCH_2OCO_2Li, P=O species and Li_2CO_3 were formed. Thus, the RCH_2*O*CO_2Li (~533.5 eV) and C=O, P=O peaks show the higher intensity. After the lithiation process, a new peak corresponding to ROLi, Li_4SiO_4 (~530.5 eV) appears.[4,20,73,82,86,87] Then, after the delithiation process, this peak still exists, but shows a slightly lower intensity. The formation of silicates (Li_4SiO_4) according to reaction (18) cannot be ruled out. The RCH_2*O*CO_2Li (~533.6 eV) peak decreases, which is in agreement of C 1s core level peak where the -CH_2O*C*O_2- peak is observed.

C species C 1s	**C-H, C-C**	**C-O ether linkage**	**-OCH_3**	**O-C=O**	**-CH_2OCO_2-, Li_2CO_3**
BE (± 0.1 eV)	285.0	286.5	287.1	288.8	290.0
FWHM = 1.5 ± 0.2 eV					
O species O 1s	**Li-O**	**ROLi, Li_xSiO_y**	**C=O, P=O**	**Si-O, C-O**	**RCH_2OCO_2Li**
BE (± 0.1 eV)	528.1	530.5	531.8	532.9	533.6
FWHM = 1.6 ± 0.2 eV					
F species F 1s	**Li-F**		**SiOF**	**P-F**	
BE (± 0.1 eV)	685.0		686.8	688.1	
FWHM = 1.75 ± 0.25 eV					
S species Si $2p_{3/2}$	**Si^0**	**Si^+**	**Si^{2+}**	**Si^{4+}**	**SiO_xF_y**
BE (± 0.1 eV) Pristine sample	99.1	100.2 ΔBE= BE_{Si+}-BE_{Si0}=1.1	101.8 ΔBE= BE_{Si2+}-BE_{Si0}=2.7	103.5 ΔBE= BE_{Si4+}-BE_{Si0}=4.4	-
BE (± 0.1 eV) Cycled samples	97.8	99.3 ΔBE= BE_{Si+}-BE_{Si0}=1.5	100.8 ΔBE= BE_{Si2+}-BE_{Si0}=3.0	102.9 ΔBE= BE_{Si4+}-BE_{Si0}= 5.1	104.7 ΔBE= BE_{SiOxFy}-BE_{Si0}= 6.9
FWHM (eV)	1.0 ± 0.2	1.6 ± 0.2			

Table 1. Binding energies (BE) and full width at half maximum (FWHM) of different species in C 1s, F 1s, O 1s and Si 2p XPS spectra.

2.1.3 SEI layer evolution in EC-DMC, DMC and PC-based electrolytes

To discuss the surface modifications of the Si electrode, the evolution of the amount of Si was measured by XPS on the Si thin film pristine electrode surface and at different stages of lithiation and delithiation of Si in three electrolytes. To do so the atomic percentage of Si (a total Si 2p core level signal) was calculated. From the Si 2p intensity variation (as observed in Figure 2 and S2), the SEI thickness modifications can be deduced. As discussed above after formation of SEI layer (C2) or at lithiated state (A1), the principal Si 2p components are the Si oxide and Si fluoride species, which are difficult to be distinguished due to their close binding energies and problems of overlapping.[73,76] Thus, the changes of Si-related species on the Si electrode as a function of different electrolytes are not straightforward. However, it can be concluded that the SEI layer is not stable during the first cycle of lithiation and delithiation in these three electrolytes and undergoes thickening and thinning, respectively (as shown in Figure S2). At the end of the delithiation process the Si 2p signal is considerably attenuated compared with the C1 point confirming the irreversible surface modifications after the first cycle. A similar behavior was observed on the nanosilicon composite electrodes cycled in $LiPF_6$/EC-DEC.[3,11,64,88] This dynamic behavior of the SEI layer, showing its thickening and thinning during lithiation and delithiation, respectively, was also observed on the other types of negative electrode materials.[52]

To compare other surface components than the Si-related components formed on Si electrodes cycled in 3 different electrolytes (1 M $LiPF_6$/EC-DMC, 1 M $LiPF_6$/DMC and 1 M $LiPF_6$/PC), the relative intensity ratios for C 1s, F 1s and O 1s peaks were calculated for different lithiation/delithiation potentials (C1-C4, A1, A2) (Figure 3). The details of peak decompositions are shown in supplementary information (Figure S3, S4 and S5). From Figure 3 for C 1s peak, it can be observed that the major species formed on the Si electrode cycled in 1 M $LiPF_6$/EC-DMC are RCH_2OCO_2Li, Li_2CO_3, $-OCH_3$ and C-O ether link, which are typical species originated from an electrochemical decomposition of EC and DMC solvents according to the reactions (1)-(4), (9), (10), (19) and (20).[20,41,80,84,85,87] The main species on the Si electrode cycled in 1 M $LiPF_6$/DMC is $-OCH_3$, due to the electrochemical decomposition of

DMC according to reaction (3).[20,41] The quantity of RCH_2OCO_2Li species is lower and no signal of C-O ether link (~286.5 eV) is observed on Si sample cycled in 1 M $LiPF_6$/DMC in comparison to the other two electrolytes. The ether species are clearly evidenced in PC- and EC-DMC-based electrolytes in agreement with previous works.[82,89] It is reported that $LiPF_6$ could react with solvents EC and DMC differently according to the reactions (8), (11), (12), (19) and (20).[84,85] A component with C-O ether link could form in the electrolyte with ring EC structure but could not form with only linear DMC molecules, which supports the XPS results. The electrode in 1 M $LiPF_6$/PC also shows C-O ether link during the cycling. Thus, the reaction (21) between $LiPF_6$ and ring structure PC molecules could be inferred. On the surface of Si electrode cycled in 1 M $LiPF_6$/PC, the peaks corresponding to RCH_2OCO_2Li, Li_2CO_3, according to electrochemical reactions (6) and (7), increase during the lithiation and then decrease during the delithiation, indicating that the thickness of the SEI layer changes.

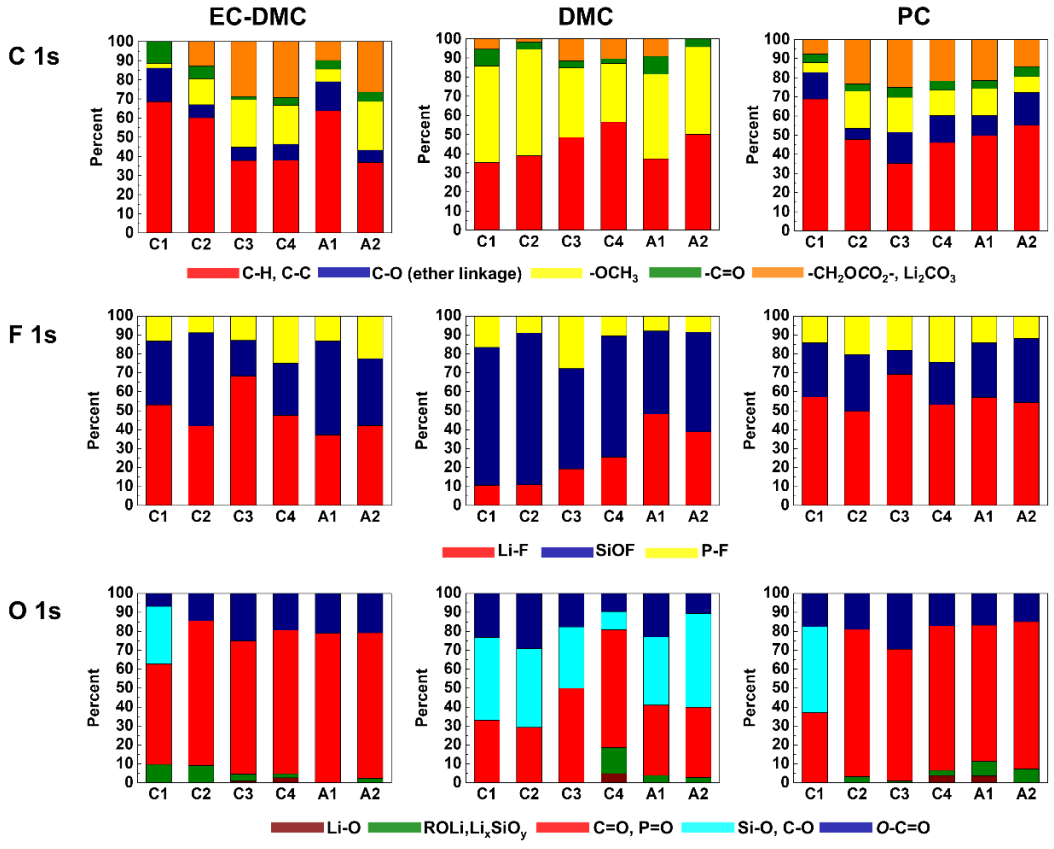

Figure 3 A comparative analysis of relative intensity ratios of different species for C

1s, F 1s and O 1s core levels peaks obtained for Si electrodes lithiated and delithiated at different potentials (C1-C4, A1, A2) in three different electrolytes (1 M $LiPF_6$/EC-DMC, 1 M $LiPF_6$/DMC and 1 M $LiPF_6$/PC).

Looking at the presence and relative intensity ratios of F-like components (F 1s profiles in Figure 3), the SiOF signal is the principle peak on the electrode cycled in 1 M $LiPF_6$/DMC, while the Li-F is the principle peak on the electrode cycled in 1 M $LiPF_6$/EC-DMC and 1 M $LiPF_6$/PC. The SiOF signal can be attributed to the formation of SiO_xF_y on the bulk electrode material.[90,91] Therefore, the SiOF signal decrease can be attributed to the increase of the SEI layer thickness. On the other hand, the volume variations of Si during the lithiation and delithiation processes could lead to the fracture of the SEI layer and the exposition of the Si electrode not covered by the SEI layer. The SiOF signal can be a fingerprint of these new revealed parts of the Si electrode. Therefore, it is difficult to firmly conclude about the changes of SiOF signal as a function of lithiation/delithiation as the signal intensity can be influenced by a modified morphology of the Si electrode (e.g. the increased roughness). However, it can be observed a clear tendency for PC and EC-DMC electrolytes showing a decrease of SiOF signal intensity with lithiation and increase with delithiation confirming a thickening and thinning of the SEI layer, respectively, as discussed above. The highest relative intensity of SiOF signal observed for DMC electrolyte can confirm the formation of the thinner SEI layer than in the other two electrolytes.

In the O 1s profiles (Figure 3), the Si-O signals could be only observed at the beginning of lithiation corresponding to decomposition of electrolyte (point C1) on the electrodes cycled in 1 M $LiPF_6$/EC-DMC or 1 M $LiPF_6$/PC. Then, the Si-O signal disappears suggesting that the surface of Si electrode is covered by a thick SEI layer, while the Si-O signal is well observed during the whole cycle on the electrode cycled in 1 M $LiPF_6$/DMC, demonstrating a formation of thinner SEI layer. After the full lithiation (C4), the Si electrode can undergo a huge volume change which results in some cracks on the SEI layer. Thus, a small Li_2O signal near the Si surface is detected, and then disappears when the volume change decreased after delithiation (A2) in

these three different electrolytes. The formation of Li_2O can be according to reaction (16).[88] On the electrode with 1 M $LiPF_6$/DMC, -OCH_3 becomes the main species at the lithiated state (point C4) as already confirmed from decomposition of C 1s peak, while the Si-O signal becomes lower, indicating the thicker SEI layer at this point.

2.1.4 SEI layer evolution with cycling

Figure 4 shows the C 1s, F 1s and O 1s core level spectra for Si electrodes obtained after 5 cycles (CV) at delithated state in three different electrolytes (1 M $LiPF_6$/EC-DMC, 1 M $LiPF_6$/DMC and 1 M $LiPF_6$/PC). Comparing with the XPS spectra after the delithation stage of the first cycle (point A2, shown in Figure S3, S4 and S5), the shapes of the spectra on the electrode with 1 M $LiPF_6$/PC do not show significant changes, but the intensities of F 1s peak decrease significantly. It demonstrates that the ratios of fluorine-related components decrease in the SEI layer after 5 cycles. On the electrode with 1 M $LiPF_6$/DMC, the shape of the F 1s and O 1s spectra after 5 cycles are similar to those after the first cycle, illustrating that the thickness of the SEI layer on the electrode does not change significantly. The C 1s peak shows a significant difference with a -OCH_3 relative intensity decrease, while a C-O ether linkage peak (~286.5 eV) and a small -CH_2OCO_2-, Li_2CO_3 peak (~290.0 eV) appear, which can be attributed to the reactions (5) and (8).[41,80,87] On the electrode with 1 M $LiPF_6$/EC-DMC, the shape of O 1s after 5 cycles is nearly the same as that after the first cycle, while the SiOF and P-F relative intensities decrease in the F 1s region, indicating that the SEI layer becomes thicker and more LiF is generated instead of P-F. The C 1s peak shows the C-O ether linkage ratio increases, while the -OCH_3 and -CH_2OCO_2-, Li_2CO_3 relative intensities decrease. It demonstrates that more polymers with C-O ether linkage are formed instead of CH_3OLi, RCH_2OCO_2Li and Li_2CO_3 on the surface.[84,85]

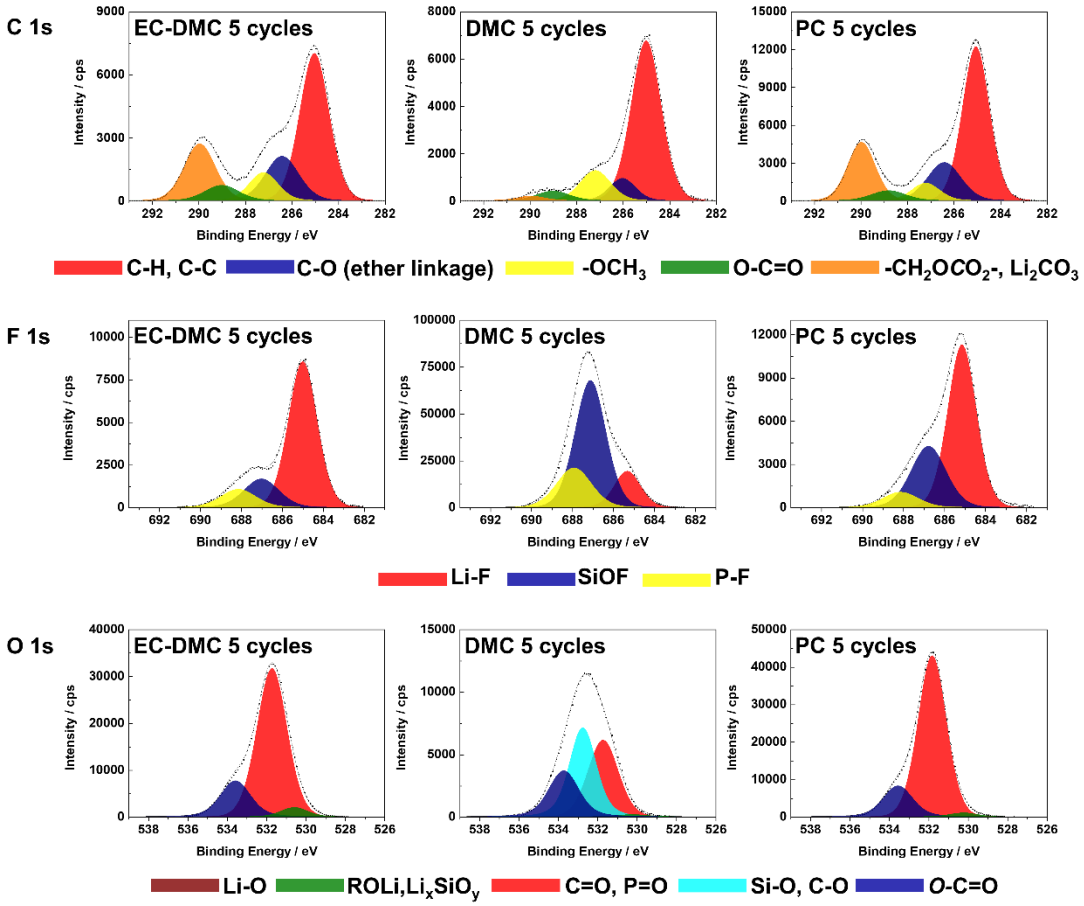

Figure 4 High resolution C 1s, F 1s and O 1s core level spectra obtained for Si electrodes after 5 CV cycles in three different electrolytes (1 M $LiPF_6$/EC-DMC, 1 M $LiPF_6$/DMC and 1 M $LiPF_6$/PC).

2.2 Surface and bulk thin film Si electrode modifications by ToF-SIMS ion depth profiles

To have a better insight into the surface and bulk modifications of Si thin film electrode material induced by lithiation and delithiation process in the three different electrolytes a ToF-SIMS in depth profile analysis was performed at fully lithiated (0.01 V) and delithiated (3.0 V) states. First, the ToF-SIMS ion depth profiles (expressed as a function of sputtering time) are presented for the pristine Si thin film (Figure 5(a)) and then compared with fully lithiated (Figure 5(b)) and delithiated (Figure 5(c)) samples in $LiPF_6$/DMC electrolyte. The used sputtering conditions and specifically the sputtered area (300 μm*300 μm) are optimized to get a sufficiently

high sputtering rate to be able to reach the Cu substrate, while maintaining a sufficiently high depth resolution to have a good overview of surface as well as bulk modifications of Si electrode material. The intensities are shown with a logarithmic scale in order to magnify the low intensity signals.

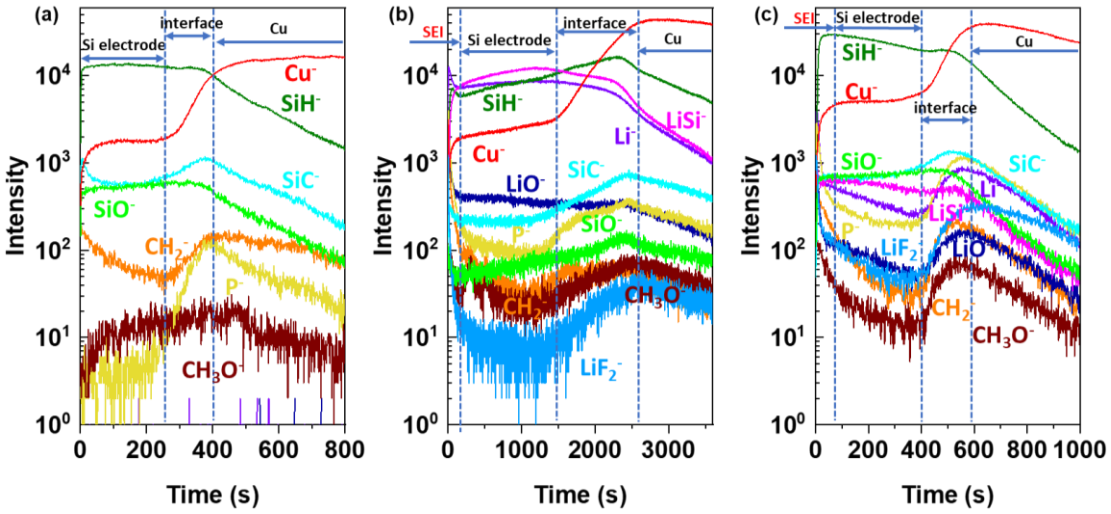

Figure 5 ToF-SIMS negative ion depth profiles for (a) pristine Si thin film; (b) Si electrode after half CV cycle in $LiPF_6$/DMC; (c) Si electrode after a full CV cycle in $LiPF_6$/DMC (sputtering area 300 μm*300 μm, CV scan rate 0.2 mV s^{-1}).

For the pristine Si thin film electrode (Figure 5(a)), the stable intensities of SiH^- and SiO^- in the beginning 255 s of sputtering can be attributed to a homogenous Si thin film distribution over the sputtered depth. Then, between 255 s and 400 s, one enters the interfacial region between Si thin film and Cu substrate, where an obvious increase of Cu^- signal and decrease of SiH^- and SiO^- signals are observed. In the interfacial region, the maximum intensity for SiC^-, P^- and CH_2^- signals (attributed to Si electrode material and some electrode and/or Cu substrate contaminations) can be observed. These intensities increase in the interfacial region can be explained by enrichment in carbon, hydrocarbon and phosphorus-like contaminations on the surface of Cu substrate (current collector). For longer sputtering times (over 400 s), the Cu^- intensity becomes high and stable while all other signals are decreasing, indicating that the Cu substrate is reached.

Figure 5(b) shows the ion depth profiles of Si thin film electrode after half CV cycle performed in $LiPF_6$/DMC. Comparing with the pristine Si, the significant increased intensities of organic (CH_3O^- and CH_2^-), lithium (Li^-, LiF^-, LiO^- and $LiSi^-$) and P^- related species, illustrate the formation of SEI and the diffusion of electrolyte decomposition products into the Si film. The presence of organic (C-H- like components) and inorganic (Li-containing components) is in agreement with XPS results discussed above. The high intensity of organic and inorganic components is particularly observed for around first 200 s of sputtering time. Appearance of new $LiSi^-$ signal showing a high intensity over the long sputtering time (up to ~1500 s), confirms the formation of Li_xSi alloy. The decrease of the SiO^- and SiC^- intensity can be also attributed to the formation of Li_xSi alloy.

The sputtering time to reach the interfacial region increases from about 255 s (for pristine Si electrode, Figure 5(a)) to about 1400 s (for lithiated Si electrode, Figure 5(b)), demonstrating the increase of thickness of Si thin film electrode material related to volume change and the pulverization of Si electrode after lithiation. The increase of sputtering time is higher than 5 times indicating huge electrode modifications. This strong increase of sputtering time can be also related to changes in the electrode composition (formation of Li_xSi alloy), i.e. a slower sputtering yield of the lithiated sample than the pristine sample. The significant increase in the sputtering time is also observed for the interfacial region (from around 150 s for the pristine sample to over 1000 s for the lithiated sample) which can be related to the roughness increase induced by formation of Li_xSi alloy. Similar huge increase of interfacial region of Si thin film electrode after electrochemical treatment has also been observed by energy-dispersive X-ray (EDX) analysis according to previously published paper.[92]

Figure 5(c) shows the Si electrode after a full CV cycle performed in $LiPF_6$/DMC. The sputtering time to reach the interface region decreases to around 400 s, indicating the Si electrode contraction. However, the electrode contraction is not completely reversible as it can be deduced from the lower sputtering time of Si pristine electrode (around 255 s). The irreversible process of delithiation can be explained by some Li trapping in the Si thin film electrode material,[33,56] which can

also be confirmed from the relatively high intensity of $LiSi^-$ signal in the delithiated sample. The intensities of CH_3O^- and CH_2^- decrease in the bulk Si in comparison to lithiated Si electrode (Figure 5(b)) but not on the surface confirming the presence of SEI layer on the electrode surface after delithiation. A significant decrease of SEI sputtering time for the delithiated sample (around 30 s) in comparison to lithiated sample (200 s) is observed, indicating the thinning of the SEI layer. This dynamic behavior of the SEI layer with the increase and successive decrease of the SEI layer was previously reported for Si-based[64,93] and conversion–type negative electrodes.[94]

In order to better observe and understand the surface modifications and the composition of SEI layer on the Si electrodes cycled in different electrolytes after half and full CV cycle, ToF-SIMS depth profiling with lower sputtering rate (by enlarging the sputtering area from 300 μm*300 μm to 500 μm*500 μm) are obtained, as shown in Figure 6. The ion depth-profile intensities obtained after half and the full CV cycles were normalized by the Cu^- signal, which becomes stable in the Si electrode region, respectively, assuming that the Cu signal is not affected by the lithiation and delithiation processes. As the variations of SiC^-, SiO^-, Cu^- and P^- ion depth profiles are more obvious when the faster sputtering rate was applied (Figure 5) than for slower sputtering rate (Figure 6), thus these profiles are not shown in Figure 6. The results presented in Figure 6 show significant differences in the ion profile shapes and their intensities after half and full cycle.

For the lithiated (after half cycle, Figure 6) Si electrodes, a high intensity of Li^- signals can be observed indicating the formation of Li-Si phase. The high Li^- signal intensity over 300 s indicates that the Cu substrate was not reached, contrary to the Li^- ion profiles showed in Figure 5 (b) where a decrease of this ion signal can be observed at around 2300 s. In the first 20-25 s of sputtering of lithiated samples (Figure 6), the peaks and then the abrupt decreases of lithiated species (LiO^-, $LiSi^-$, and LiF_2^-) are observed. However, the Li^- signal has not the same shape at the beginning of sputtering. Thus, these LiO^-, $LiSi^-$, and LiF_2^- peaks can be ascribed to uneven morphology of the Si electrode induced by lithiation and huge volume

changes of Si and resulting in patchy surface layer. The LiO^- profile shows a small peak in the first 25 s, indicating the presence of oxide layer on the extreme surface. After 20-25 s, the Li-related (Li^-, LiO^-, $LiSi^-$, and LiF_2^-) and organic-related (CH_2^- and CH_3O^-) signals exhibit different shapes as a function of sputtering time, indicating different species distributions in the SEI layer. In the inner part of the SEI layer a slow intensity decrease of LiO^- signal (more or less important depending on the electrolyte) indicates a relatively homogenous distribution of LiO-related species over the SEI. At the minimum intensity of $LiSi^-$ signal (at around 25 s of sputtering), the maximum intensity of CH_2^- and CH_3O^- signals corresponding to organic species can be observed indicating that the concentration of organic species decreases and is smaller in the inner part of the SEI layer close to lihitated Si electrode. The LiF_2^- profiles corresponding to LiF salt show the maximum intensity peak at the same sputtering time as the LiO^-, $LiSi^-$ and profiles indicating the uneven morphology caused by the huge volume changes leads to revealing some species attributed to the inner layer. After reaching the maximum intensity, a significant slope in the LiF^- profile can be observed with a higher decreasing rate than for the LiO^- profile, indicating that these species are present principally in the outer part rather than in the inner part of SEI layer. After 200-250 s, SiH^- and $LiSi^-$ profiles become relatively stable, indicating the sputtering reaches the Si lithiated electrode.

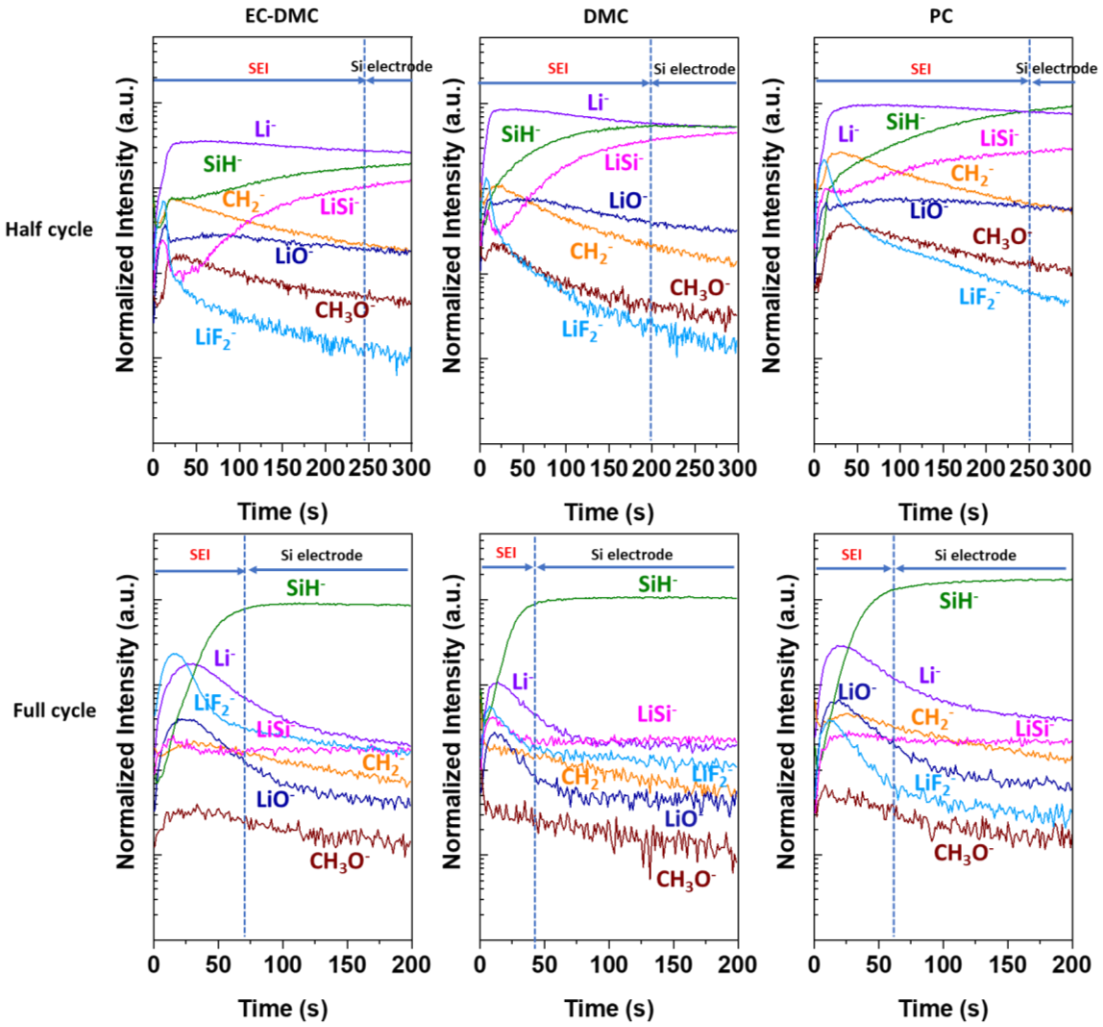

Figure 6 ToF-SIMS negative ion depth profiles Si thin film electrode after half and full CV cycle (scan rate 0.2 mV s^{-1}) in $LiPF_6$/EC-DMC, $LiPF_6$/DMC and $LiPF_6$/PC electrolyte, respectively. Sputtering area 500 µm * 500 µm.

For the lithiated samples it is difficult to discuss the surface and bulk differences in chemical composition induced by different electrolytes. However, some differences in the signal ratios can be observed. The CH_2^- signal is higher than LiO^- signal up to 200 s on the electrode with $LiPF_6$/EC-DMC and $LiPF_6$/PC, while the CH_2^- signal becomes lower than the LiO^- signal at 55 s on the electrode cycled in $LiPF_6$/DMC, illustrating the differences of the SEI layer composition. More important differences can be observed as function of the sputtering time in the different electrodes. In the case of Si electrode cycled in $LiPF_6$/DMC a more rapid increase of SiH^- signal to high intensity than in the other two electrolytes, leading to intersection with Li^- ion profile

at around 200 s, is observed. This intersection point can be considered as the limit of the SEI layer and the beginning of lithiated Si electrode where a more stable $LiSi^-$ signal intensity is observed. The intersection of SiH^- and Li^- ion profiles is shifted to higher sputtering time (~250 s) for Si electrode cycled in $LiPF_6$/PC and no intersection can be observed for Si cycled $LiPF_6$/EC-DMC indicating much thicker SEI layer in these two electrolytes. However, it should be noted that the sputtering time increase of the interface region can be also affected by more significant morphological modifications induced by lithiation and material pulverization as already demonstrated before.[24,95]

It can be concluded from these results that the SEI layer has a LiF-like and organic-rich thin outer layer. The inorganic LiO-species can be found in SEI layers as well as in the bulk of the lithiated Li_xSi phase. The thinnest SEI layer was observed on the surface of Si electrode cycled in $LiPF_6$/DMC electrolyte.

After the full cycle of lithiation and delithiation (Figure 6), the principal high intensity signal observed in the bulk delithiated Si electrode is SiH^-. In the case of all three electrolytes, similar shapes and relative intensity signals can be observed in the second region corresponding to the area of Si delithiated electrode and they are similar to the pristine electrode (Figure 5 (a)). In comparison to the pristine electrode, in the bulk of delithiated samples the higher intensity of Li^-, LiO^-, LiF_2^- and most particularly $LiSi^-$ are observed. However, delithiation lead to lowering the $LiSi^-$ signal intensity when comparing to the lithiated samples due to removal of most of the lithium. The other compounds related to products of electrolyte decomposition (CH_2^- and CH_3O^-) diffuse into the bulk of the electrode and are trapped in the electrode's structure.

More significant modifications of the delithiated samples comparing with the lithiated samples can be observed in the first region related to the SEI layer. The LiO^- signal shows the same shape as Li^- signal confirming the presence of Li_2O in the SEI layer. The higher quantity of Li_2O can be observed on the surface of Si electrode cycled in $LiPF_6$/EC-DMC and $LiPF_6$/PC than on the Si electrode cycled in $LiPF_6$/DMC. The presence of Li_2O is a result of reaction (16) and it was already

confirmed by XPS on the lithiated samples.

Together with a high intensity of Li^-, LiF_2^- and LiO^- signals, a decrease of organic species such as CH_3O- and CH_2- like species can be observed after delithiation with more homogenous in-depth distribution (in the SEI layer and in the delithiated Si electrode region), indicating the presence of some organic species in the SEI layer after delithiation.

Here from the intensity changes of signals as a function of sputtering time, the apparent differences in the SEI layer thickness can be also evidenced. As aforementioned, the influence of the increased roughness induced by the morphological changes (cracks, pulverization) on the shape of ion profiles and then related to its increased sputtering time cannot be ruled out. Considering that the delithiated Si electrode was reached after reaching the stable intensity of the SiH^- signal, the region before the plateau of SiH^- can be attributed to the SEI layer. This region is characterized by the high intensity of Li^-, LiF_2^- and LiO^- signals and also slightly higher signal of CH_3O^- and CH_2^-. As illustrated on the lithiated samples, the lowest sputtering time for the SEI layer present on the delithiated sample is observed for the Si electrode cycled in $LiPF_6$/DMC electrolyte (~45 s) in comparison to ~60-70 s for the other two electrolytes. The SEI layer on all delithiated samples is considerably thinner than on the lithiated samples. These results are in agreement with previously published research [24,95]. The SEI double-layered structure (with the outer and inner layer) is less evident on the surface of delithiated than lithiated samples.

2.3 Influence of lithiation/delithiation to the electrolyte components by *in situ* MFTIRS

2.3.1 Cyclic voltammetry of Si thin film electrode during *in situ* MFTIRS

The *in situ* MFTIRS was adopted to illustrate the molecular level of the interface chemistry. The shapes of the CV performed in three different electrolytes (1 M $LiPF_6$/EC-DMC, 1 M $LiPF_6$/DMC and 1 M $LiPF_6$/PC) are similar thus only the result for the Si electrode cycled in 1 M $LiPF_6$/EC-DMC is shown in Figure 7(a) as an example. This CV curve exhibits more peaks during the cathodic process than those

curves shown in Figure 1 because of its lower scan rate and different cell geometry. Before lithiation taking place, a single beam spectrum was recorded at the reference potential E_R and then, the other single beam spectrums were collected at different cathodic (C1-C3) and anodic (A1-A4) potentials during lithiation and delithiation processes, respectively. The selected *in situ* MFTIR spectra (at C1, C3, A1 and A3 points) focusing on the changes of C=O and C-H bonds are shown in Figure 7(b)-(d). The detail *in situ* MFTIR spectra from 800-2000 cm^{-1} at all cathodic and anodic potentials are shown in Figure S7-S9, respectively.

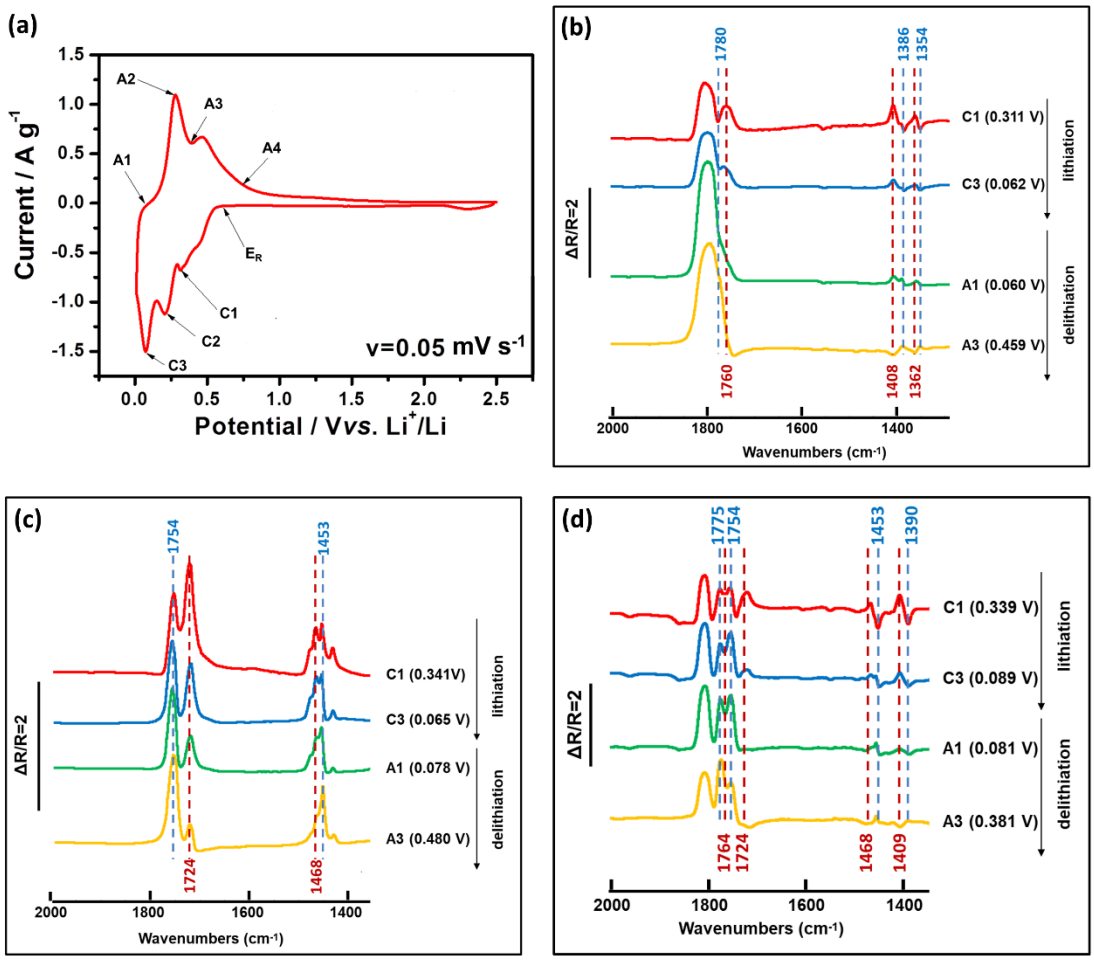

Figure 7 (a) The first cycle CV of Si electrode tested in 3-electrode *in situ* MFTIRS cell in 1 M $LiPF_6$/EC-DMC (scan rate v = 0.05 mV s^{-1}). The *in situ* MFTIR spectra of Si electrode in (b) 1 M $LiPF_6$/PC (E_R = 0.611 V), (c) 1 M $LiPF_6$/DMC (E_R = 0.590 V) and (d) 1 M $LiPF_6$/EC-DMC (E_R = 0.671 V) at C1, C3, A1 and A3 points during the first CV cycle.

2.3.2 *In situ* MFTIRS

Previous research shows that Li ions could solvate with carbonate solvent molecules resulting in the formation of $Li(sol)_n^+$ species (sol: EC, DMC and PC).[21,96,97] The schematic molecular structure of Li^+ solvated carbonates are shown in Figure S6. During this process, the coordination of Li^+…O=C may lead to the weaken of C=O bond in the $Li(sol)_n^+$ species, resulting in the red shift of the $\nu_{C=O}$ of $Li(sol)_n^+$ related to the free solvent molecules, respectively.[21,98,99] During the lithiation process, the desolvated Li^+ ions from $Li(sol)_n^+$ complex could alloy with Si, as the result, the free solvent molecules will increase and the amount of $Li(sol)_n^+$ species decrease.

Figure 7(b) shows the spectra of the Si electrode with cyclic carbonate solvent PC during the first CV cycle. The spectra are calculated according to the definition of ΔR/R recorded at different E_S values during the first lithiation and subsequent delithiation processes. Here E_R was chosen at 0.611 V. The lithiation and delithiation was accompanied with the reduction of the thin-layer electrolyte between the IR window and Si electrode, indicating by the presence of obvious downward/upward of IR bands in the spectra. The band at 1780 cm^{-1} is assigned to the stretching vibration of C=O. Due to the solvation of PC with Li ions, this band is shifted to 1760 cm^{-1} towards the low frequency end.[48,100] The intensity of the upward band at 1780 cm^{-1} correlating to free PC decreases during the lithiation process and then increases during the delithiation process. The intensity of the upward band at 1760 cm^{-1} correlating to $Li(PC)_n^+$ shows an opposite trend. It increases during the lithiation process, decreases during the delithiation process and becomes downward at 0.660 V of delithiation. The peak at 1386 cm^{-1} is attributed to the scissoring vibration of CH_3 and the wagging vibration of O-CH_2 of PC. The peak at 1354 cm^{-1} is assigned to the bending vibration of the PC ring and the symmetric bending vibration of CH_3 of PC. Due to the solvation of PC with Li ions, the original bands at 1386 and 1354 cm^{-1} are shifted to 1408 and 1362 cm^{-1} towards the high frequency end.[100] The upward peaks during the lithiation process at 1408 and 1362 cm^{-1} correlating to $Li(PC)_n^+$ change to downward

peaks during the delithiation process. The downward peaks during the lithiation process at 1386 and 1354 cm^{-1} corresponding to free PC change to upward peaks during the delithiation process. It demonstrates that during the lithiation, $Li(PC)_n^+$ decreases with a decrease in potential, while the free PC increases. During the delithiation process, free PC decreases with an increase in potential, while $Li(PC)_n^+$ increases. In a diffusion double layer, it has been assumed that a decrease in the potential causes an increase in the cation concentration, as well as a decrease in the anion concentration, and the ion concentrations change with an opposite trend when the potential increases. Therefore, an intensity growth at 844 cm^{-1} (PF_6^-) is observed in Figure S7 during the lithiation process. It decreases during the delithiation.

Similar experiment has been performed on Si electrode with linear carbonate solvent DMC, as shown in Figure 7(c). The peaks at 1754 cm^{-1} and 1724 cm^{-1} can be correlated with the $\nu_{C=O}$ of unsolvated DMC and $Li(DMC)_n^+$, respectively.[46,101] The upward band of 1724 cm^{-1} correlating with the $\nu_{C=O}$ of $Li(DMC)_n^+$ decrease obviously during the delithiation process, indicating the increase of $Li(DMC)_n^+$ concentration. When the Li ions extract from the Li-Si alloy, Li ions will solvate with free solvent molecules. In the same case, the peak corresponding to C-H of $Li(DMC)_n^+$ at 1468 cm^{-1} increases during the lithiation process and decrease during the subsequent delithiation, since $Li(DMC)_n^+$ concentration decrease when Li^+ alloy with Si and then increase when Li ions extract from the Li-Si alloy. The peak at 1453 cm^{-1} corresponding to C-H of free DMC shows an opposite trend of intensity variety comparing with the peak at 1468 cm^{-1}. In Figure S8, the peaks correlating to ν_{C-O} of free DMC and the peak of $Li(DMC)_n^+$ species can be found at 1274 cm^{-1} and 1319 cm^{-1}, respectively.[101] The upward peak of ν_{C-O} for $Li(DMC)_n^+$ at 1319 cm^{-1} is found enhanced during lithiation process and weaken during lithiation process. The peak correlating to PF_6^- can be observed at 844 cm^{-1}.

For experiment performed on Si electrode with mixed solvent EC-DMC, E_R was chosen as 0.617 V. The results are shown in Figure 7(d). The upward peak at 1775 cm^{-1} corresponding to $\nu_{C=O}$ of free EC and the downward peak at 1764 cm^{-1} corresponding to $\nu_{C=O}$ of $Li(EC)_n^+$ decrease during the lithiation process,[102] and then

increase during the delithiation process. It demonstrates that the concentration of free EC increase during the lithiation and decrease during the delithiation, while the concentration of $Li(EC)_n^+$ exhibits the opposite changing trend during the first CV cycle. However, the upward peak corresponding to $Li(DMC)_n^+$ at 1724 cm^{-1} decreases during the lithiation and changes to be a downward peak during the delithiation.[102] Thus, EC plays the main role to coordinate with Li ions in the electrolyte. The upward peaks at 1409 and 1468 cm^{-1} correspond to C-H of $Li(sol)_n^+$.[46,101] The downward peaks at 1390 and 1453 cm^{-1} corresponds to C-H of solvent molecules. To ensure the balance of electric during the Li^+ alloying process with Si electrode, an obvious 842 cm^{-1} upward peak was found in Figure S9, correlating with PF_6^- anions.[29]

Comparing the intensities of *in situ* MFIRS ($\Delta R/R$) on the Si electrode with these three electrolytes, the Si electrode with $LiPF_6$/DMC shows less significant change during the lithiation and delithiation processes, illustrating that fewer DMC molecules take part in the interfacial reactions, which probably results in a thinner SEI layer on the electrode.

2.4 Morphological modifications of Si thin electrodes as a function of electrolyte

The morphology and composition of the SEI layer depend strongly on the electrolyte components. Figure 8 shows SEM micrographs of Si thin film electrode after 1 CV cycle and 5 CV cycles in different electrolytes and for comparison the pristine sample is shown in Figure S10(a). After one complete cycle in $LiPF_6$/EC-DMC the Si electrode (Figure 8(a)) exhibits several slight cracks. A homogeneous surface is shown on the Si electrode cycled in $LiPF_6$/DMC (Figure 8(c)), while the surface of Si electrode cycled in $LiPF_6$/PC ((Figure 8(e)) is more uneven. After 5 CV cycles, the Si electrode cycled in $LiPF_6$/DMC still exhibits a homogeneous surface ((Figure 8(d)), while the Si electrodes cycled in $LiPF_6$/EC-DMC ((Figure 8(b)) and $LiPF_6$/PC (Figure 8(f)) show many deep cracks.

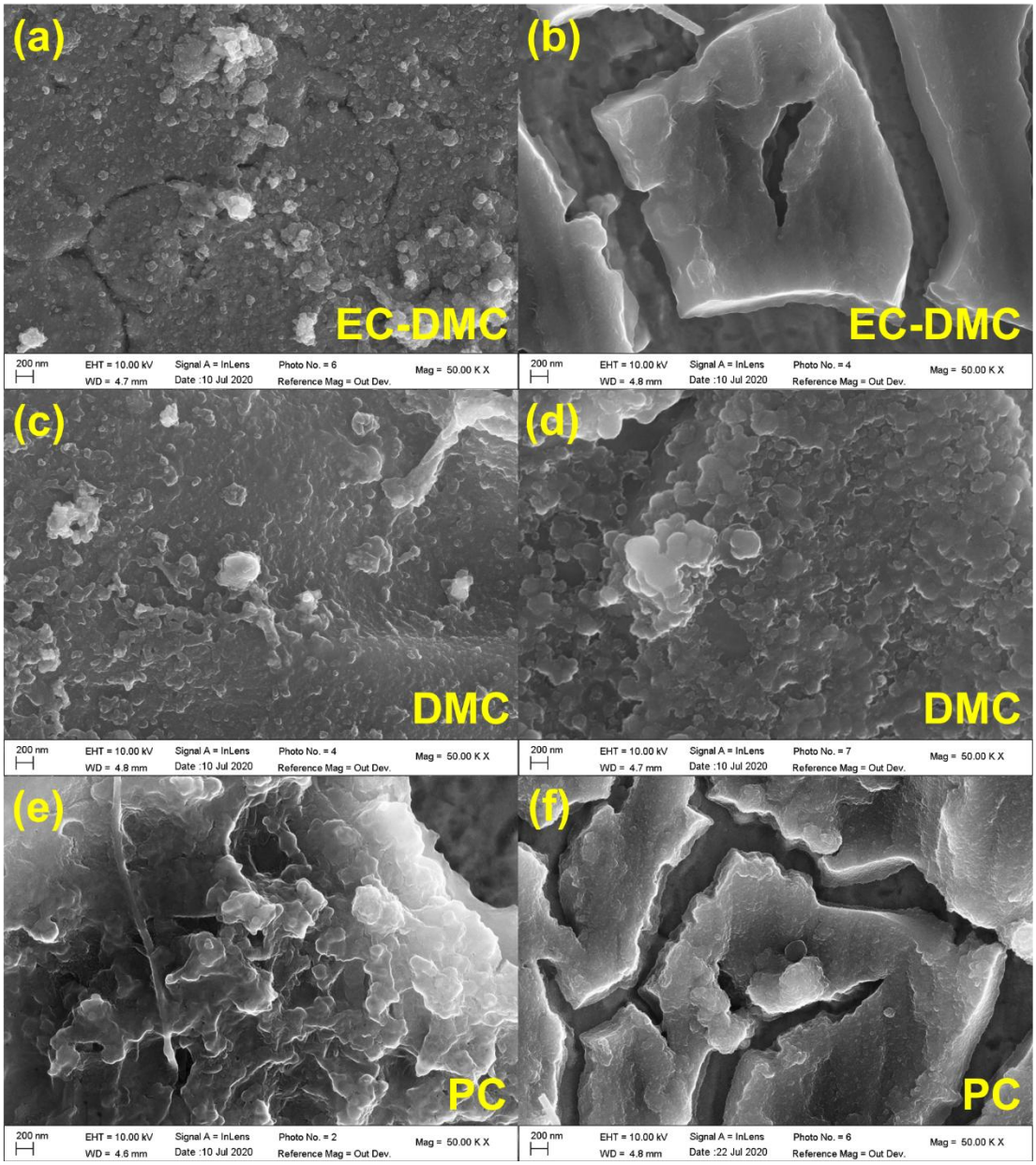

Figure 8 Morphology of Si electrodes with (a)(b) $LiPF_6$/EC-DMC, (c)(d) $LiPF_6$/DMC and (e)(f) $LiPF_6$/PC after the 1 CV cycle (left) and 5 CV cycles (right) in the Swagelok cells (scan rate 0.2 mV s^{-1}).

2.5 Galvanostatic charge-discharge test of Si thin film electrode in different electrolytes

Galvanostatic charge-discharge tests of the Si electrode with different electrolytes were performed to investigate the influence of the electrode solvents on capacity retention (Figure 9). The Si electrode cycled in $LiPF_6$/DMC electrolyte

exhibits an initial charge capacity of 2704.5 mAh g^{-1} and a capacity retention of 77.2% after 60 cycles. However, the employment of $LiPF_6$/EC-DMC electrolyte resulted in lower initial charge capacity (2532.3 mAh g^{-1}) and capacity retention (47.7%). A higher initial capacity of 3074.1 mAh g^{-1} was observed in $LiPF_6$/PC however with a low capacity retention of 40.4% after 60 cycles. The electrode cycled in $LiPF_6$/EC-DMC shows unstable coulombic efficiency, while the electrodes cycled in other two electrolytes show relatively stable and similar coulombic efficiencies. The better cycle performance in $LiPF_6$/DMC also demonstrates that this electrolyte is beneficial to form of a good interface layer on the Si electrode.

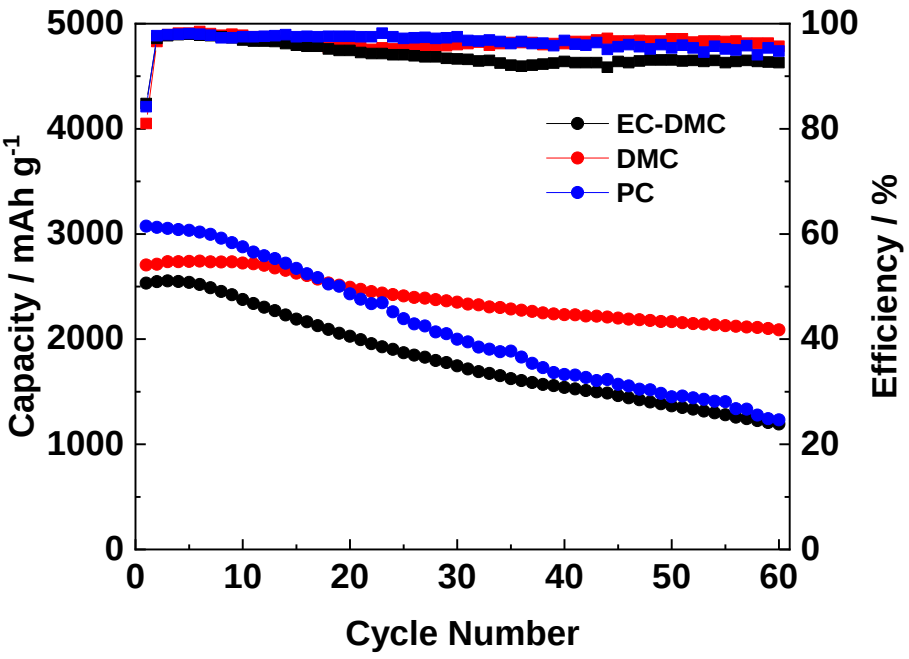

Figure 9 Cycle performance of Si electrode in different electrolytes at current density of 0.1 C.

2.6 Summarizing discussion

To summarize, the ToF-SIMS data converge well with the XPS data showing the existence and content changes of -OCH_3, -SiO, -LiF species on the surface of Si thin film electrode. At the same time in electrolyte, the *in situ* MFTIRs illustrates also the species changes. The combination of these *ex situ* and *in situ* methods enables us to

demonstrate different aspects of the Si electrode surface chemistry, which are schematically presented in Figure 10. The Figure 10 shows the structure, the composition and the morphological modifications of the SEI thin film on Si thin film electrode after the complete cycle of lithiation and delithiation as a function of electrolyte composition. It can be summarized that Li_2CO_3, RCH_2OCO_2Li, $-OCH_3$, Li_2O and LiF species are commonly observed on Si surface but the quantity can vary depending on type of electrolyte. It should be noted that the $-OCH_3$ is one of the main species formed in $LiPF_6$/DMC due to presence of two $-OCH_3$ functional groups in DMC. The species with C-O ether linkage are only found on the electrodes with $LiPF_6$/EC-DMC and $LiPF_6$/PC, due to the ring structures of solvent molecules. Moreover, the ToF-SIMS ion depth profiles demonstrated that components are not homogenously distributed in depth. The inhomogeneous, double-layered structure of the SEI was easily observed after the half cycle (at the lithiation state) by ToF-SIMS profiles (Figure 6) but after the full-cycle (at the delithiation state) this double-layered structure is less evident. It indicates that the SEI layer is not stable and strongly evolves during lithiatin/delithiation process. Moreover, the composition is also changing as a function of lithiation/delithiation and types of electrolyte as discussed above. The SEI layer schema (Figure 10) demonstrates the principle findings thus a formation of double-layered structure is highlighted with the outer part enriched in LiF for all electrolytes and inner part enriched in other components which presence depend on type of electrolyte. The SEI layer is also less enriched in Li_2O after cycling in DMC-based electrolyte.

The higher intensities of SiOF and Si-O signals in F 1s, O 1s and Si 2p XPS spectra on the electrode cycled in $LiPF_6$/DMC, indicate the formation of thinner SEI layer. These results were well confirmed by differences in the shorter sputtering time by ToF-SIMS. The dynamic behavior of the SEI layer is not show here in schema (Fig.10) as only the lithiated state is demonstrated. More significant morphological modifications (cracks formation) were also observed on the electrodes cycled in $LiPF_6$/EC-DMC and $LiPF_6$/PC in Figure 10.

The electrode surface state is not stable after the first cycle and the next cycles

lead to further modifications, which can vary as a function of electrolyte. After 5 CV cycles, more LiF species are generated in $LiPF_6$/EC-DMC and $LiPF_6$/DMC. The ratio of the species with C-O ether linkage increases significantly in $LiPF_6$/EC-DMC. The peaks corresponding to Li_2CO_3, RCH_2OCO_2Li and C-O ether linkage appear on the electrode cycled in $LiPF_6$/DMC, while the ratio of $-OCH_3$ species decreases. The intensities of the peaks related to LiF and P-F species decrease in $LiPF_6$/PC. In $LiPF_6$/DMC the obvious SiOF and Si-O signals can be observed, indicating that the SEI layer does not increase after 5 cycles. In this work, a significant influence of single DMC solvent on the formation of SEI layer in comparison with EC-DMC and PC-based electrolytes is demonstrated and this shows the importance of electrolyte optimization for Si negative electrode materials.

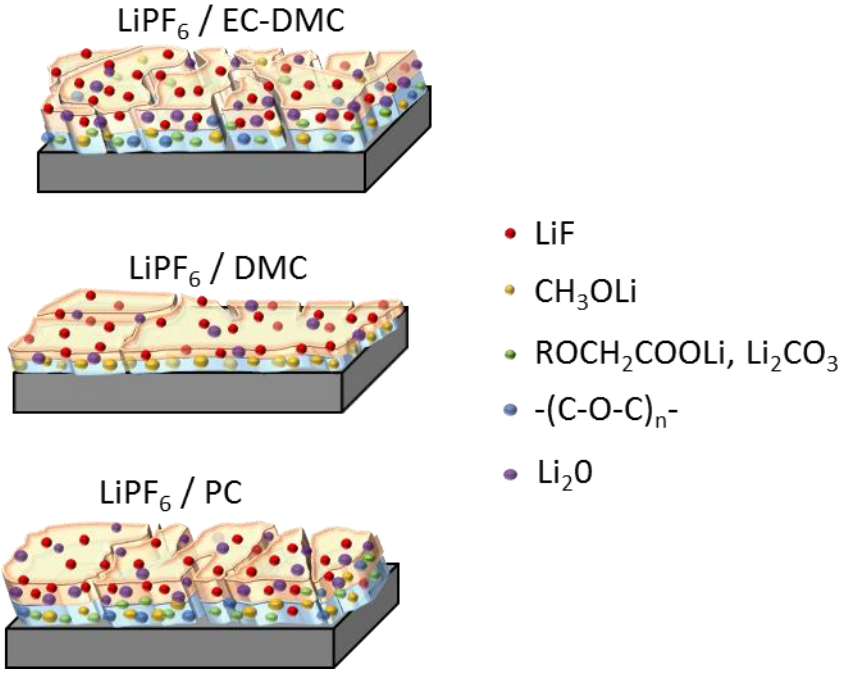

Figure 10 Schematic representation of the SEI structure and composition on Si thin film electrodes after full CV cycle in different electrolytes (1 M $LiPF_6$/EC-DMC, 1 M $LiPF_6$/DMC and 1 M $LiPF_6$/PC).

3. Conclusions

By means of *ex situ* XPS, ToF-SIMS and *in situ* FTIRS characterization of the Si thin film electrode/electrolyte interface together with SEM and galvanostatic tests, the influence of different $LiPF_6$-based carbonate solvents on the surface chemistry of Si electrode was revealed. The *ex situ* XPS and ToF-SIMS data proved a dynamic behavior of the SEI layer, showing increase and decrease thickness, induced by lithiation and delithiation, respectively, in these three different electrolytes. The stronger Si-related signals such as SiOF and Si-O in XPS profiles (Si 2p, F 1s and O 1s) showed that a thinner and more stable SEI layer is formed when the Si thin film electrode is cycled in $LiPF_6$/DMC. The *in situ* FTIRS, focused on the changes in the electrolyte near the electrode surface, demonstrated that the coordination between Li^+ and DMC was weaker and fewer DMC molecules took part in the formation of SEI layer. The morphological characterization by SEM, showed also much less cracks and lower electrode degradation when cycled in DMC-based electrolyte. Finally, the Si electrode with $LiPF_6$/DMC exhibited better cycle performance than the electrodes with other two electrolytes, in agreement with the surface characterization results.

4. Experimental part

4.1 Sample preparation

To prepare the Si electrode, JS3X-100B magnetron sputtering system was adopted to deposit a 500 nm thick Si layer on the Cu foil (20 μm thick). Before deposition, Cu substrate was washed with deionized water and acetone (Sinopharm, Chemical Reagent Co., Ltd., China). Then, the morphological characterizations of Si anode were performed by SEM (Zeiss Ultra55 microscope with high-resolution field emission gun, Schottky SEM-FEG). The crystal structure of the Si layer was checked by means of X-ray diffraction (XRD, PANalytical X'pert PRO, Philips, Cu Kα radiation).

4.2 Electrochemical tests

Three types of electrolytes were used in this study to illustrate the influence of different organic electrolytes on the formation and stability of the SEI layer: 1 M $LiPF_6$ in EC- DMC (1:1), 1 M $LiPF_6$ in DMC and 1 M $LiPF_6$ in PC. The electrolytes were purchased from Sigma Aldrich (battery grade) without further treatment.

The electrochemical measurements were performed in the Swagelok cell with Si thin film electrode as the working electrode and lithium foil (99.9% purity, Alfa Aesar) as counter electrode was used for the sample preparation. The CV measurements were performed at scan rate of 0.2 mV s^{-1} using a VMP3 Biologic multi-channel potentiostat/galvanostat. The lithiation or delithiation was stopped at different potentials during the CV tests (as detailed in results and discussion) and then these potentials were fixed for more than 10 hours in order to form a stable surface layer suitable for XPS and ToF-SIMS analyses. After the cells disassembling in the Ar-filled glove box, the cycled Si electrodes were rinsed by DMC, dried with Ar-flow and transferred directly to the XPS or ToF-SIMS analysis chamber under anaerobic and anhydrous conditions.

The *in situ* microscope FTIRS (*in situ* MFTIRS) cell (schematically illustrated in Figure S1) consisting of a KBr disk as the IR window, Si electrode as the working electrode, Li metal foil (China Energy Lithium Co., Ltd. China) as the reference and counter electrodes and electrolyte was assembled in the Ar-filled glove box. The battery grade electrolytes were purchased from Dodochem, Suzhou, China. CV measurements were performed using CHI660E electrochemical working station (Chenhua, China) simultaneously with a measurements of reflectance MFTIRS at different voltages of the first cycle were recorded.

The long-term galvanostatic cycle performance was carried out between 0.01 and 1.2 V with a current density of 0.1 C (1 C = 3580 mAh g^{-1}) at 30 ℃ in 2025 type coin cells using LAND battery testing instrument. The cells were assembled with Si thin film electrode, Celgard 2400 membrane as the separator, metallic lithium wafer as the counter electrode and different electrolytes.

4.3 X-ray photoelectron spectroscopy

XPS analysis was conducted on a ThermoElectron ESCALAB 250 spectrometer under ultra-high-vacuum (UHV) condition (under ~10^{-9} mbar) equipped with an Al Kα X-ray radiation source (hν=1486.6 eV). Spectra were taken at 90° photoelectron take-off angle. A pass energy of 100 eV and 20 eV was used to record a survey spectrum and the high resolution spectra (Si 2p, C 1s, O 1s, F 1s), respectively. Charge effects were corrected by setting the lower energy component of the C 1s peak at 285.0 eV (corresponding to C-C bonding). Peak fitting and decomposition were performed with CASA software, using a Shirley-type background and Gaussian/Lorentzian peak shapes with a fixed ratio of 70/30.

4.4 *In situ* Microscope Fourier Transform Infrared Spectroscopy

In situ MFTIRS was carried out on Thermo Nicolet Nexus iN10 FTIR spectrometer equipped with a microscope and a liquid-N_2 cooled HgCdTe detector. 400 interferograms were collected and coadded at a spectral resolution of 4 cm^{-1} to obtain every single beam spectrum. The resulting spectrum was defined according to $\Delta R/R=(R(E_S)-R(E_R))/E_R$, in which $R(E_S)$ represents the single beam spectrum collected at potential E_S and $R(E_R)$ corresponds to the single beam spectrum recorded at reference potential E_R.[44] The three-electrode cell for *in situ* MFTIRS is shown in Figure S1. The CV was performed starting with a negative scan at the scan rate of 0.05 mV s^{-1}.

4.5 Time-of-Flight Secondary Ion Mass Spectrometry

ToF-SIMS ion depth profiles were carried out at an operating pressure of 10^{-9} mbar using the ToF-SIMS 5 spectrometer (IONTOF GmbH, Munster, Germany). A 25 keV Bi^+ beam (100*100 μm^2) was used for analysis, delivering a target current of 1.2 pA. The 2 keV Cs^+ beam (300*300 μm^2 or 500*500 μm^2) was employed for sputtering, delivering a target current of 90 nA. Data acquisition and post-processing analysis were performed with Ion-Spec software (version 6.8).

5. Acknowledgements

Région Ile de-France is acknowledged for partial support for the XPS and ToF-SIMS equipment. This work is supported in part by the scholarship from China Scholarship Council (CSC) under the grant CSC N°201706310139.

6. Supporting Information

The supplementary information includes several figures such as schematic diagram of *in situ* FTIR cell, high resolution XPS spectra (C 1s, F1s and O1s) and *in situ* FTIR spectra obtained in three different electrolytes, molecular structure of three different solvents and SEM, EDS and XRD of thin film electrode.

7. Author information

Zhan-Yu Wu: wzy_cr@163.com

Yan-Qiu Lu: 819351841@qq.com

Jun-Tao Li: jtli@xmu.edu.cn

Sandrine Zanna: sandrine.zanna@chimieparistech.psl.eu

Antoine Seyeux: antoine.seyeux@chimieparistech.psl.eu

Ling Huang: huangl@xmu.edu.cn

Shi-Gang Sun: sgsun@xmu.edu.cn

Philippe Marcus: philippe.marcus@chimieparistech.psl.eu

Jolanta Światowska: jolanta.swiatowska@chimieparistech.psl.eu

Figures and tables lists

of 0.1 C.

Figure 10 Schematic representation of the SEI structure and composition on Si thin film electrodes after full CV cycle in different electrolytes (1 M $LiPF_6$/EC-DMC, 1 M $LiPF_6$/DMC and 1 M $LiPF_6$/PC).

Scheme 1. Reduction reactions on Si thin film electrode with different electrolytes (1 M $LiPF_6$/EC-DMC, 1 M $LiPF_6$/DMC and 1 M $LiPF_6$/PC).

Table 1. Binding energies (BE) and full width at half maximum (FWHM) of different species in C 1s, F 1s, O 1s and Si 2p XPS spectra.

References

(1) Meister, P.; Jia, H.; Li, J.; Kloepsch, R.; Winter, M.; Placke, T. Best Practice: Performance and Cost Evaluation of Lithium Ion Battery Active Materials with Special Emphasis on Energy Efficiency. *Chem. Mater.* **2016**, *28* (20), 7203–7217. https://doi.org/10.1021/acs.chemmater.6b02895.

(2) Obrovac, M. N.; Christensen, L. Structural Changes in Silicon Anodes during Lithium Insertion/Extraction. *Electrochem. Solid-State Lett.* **2004**, *7* (5), A93. https://doi.org/10.1149/1.1652421.

(3) Philippe, B.; Dedryvère, R.; Gorgoi, M.; Rensmo, H.; Gonbeau, D.; Edström, K. Role of the $LiPF_6$ Salt for the Long-Term Stability of Silicon Electrodes in Li-Ion Batteries – A Photoelectron Spectroscopy Study. *Chem. Mater.* **2013**, *25* (3), 394–404. https://doi.org/10.1021/cm303399v.

(4) Verma, P.; Maire, P.; Novák, P. A Review of the Features and Analyses of the Solid Electrolyte Interphase in Li-Ion Batteries. *Electrochimica Acta* **2010**, *55* (22), 6332–6341. https://doi.org/10.1016/j.electacta.2010.05.072.

(5) Zhang, W.-J. A Review of the Electrochemical Performance of Alloy Anodes for Lithium-Ion Batteries. *J. Power Sources* **2011**, *196* (1), 13–24. https://doi.org/10.1016/j.jpowsour.2010.07.020.

(6) Beattie, S. D.; Larcher, D.; Morcrette, M.; Simon, B.; Tarascon, J.-M. Si Electrodes for Li-Ion Batteries—A New Way to Look at an Old Problem. *J. Electrochem. Soc.* **2008**, *155* (2), A158. https://doi.org/10.1149/1.2817828.

(7) McDowell, M. T.; Lee, S. W.; Nix, W. D.; Cui, Y. 25th Anniversary Article: Understanding the Lithiation of Silicon and Other Alloying Anodes for Lithium-Ion Batteries. *Adv. Mater.* **2013**, *25* (36), 4966–4985. https://doi.org/10.1002/adma.201301795.

(8) Wang, K.-X.; Li, X.-H.; Chen, J.-S. Surface and Interface Engineering of Electrode Materials for Lithium-Ion Batteries. *Adv. Mater.* **2015**, *27* (3), 527–545. https://doi.org/10.1002/adma.201402962.

(9) Eshetu, G. G.; Figgemeier, E. Confronting the Challenges of Next- Generation Silicon Anode- Based Lithium- Ion Batteries: Role of Designer Electrolyte Additives and Polymeric Binders. *ChemSusChem* **2019**, *12* (12), 2515–2539. https://doi.org/10.1002/cssc.201900209.

(10) Green, M.; Fielder, E.; Scrosati, B.; Wachtler, M.; Moreno, J. S. Structured Silicon Anodes for Lithium Battery Applications. *Electrochem. Solid-State Lett.* **2003**, *6* (5), A75. https://doi.org/10.1149/1.1563094.

(11) Chan, C. K.; Ruffo, R.; Hong, S. S.; Cui, Y. Surface Chemistry and Morphology of the Solid Electrolyte Interphase on Silicon Nanowire Lithium-Ion Battery Anodes. *J. Power Sources* **2009**, *189* (2), 1132–1140. https://doi.org/10.1016/j.jpowsour.2009.01.007.

(12) Ryu, J. H.; Kim, J. W.; Sung, Y.-E.; Oh, S. M. Failure Modes of Silicon Powder Negative Electrode in Lithium Secondary Batteries. *Electrochem. Solid-State Lett.* **2004**, *7* (10), A306. https://doi.org/10.1149/1.1792242.

(13) Obrovac, M. N.; Krause, L. J. Reversible Cycling of Crystalline Silicon Powder. *J. Electrochem. Soc.* **2007**, *154* (2), A103. https://doi.org/10.1149/1.2402112.

(14) Jin, Y.; Zhu, B.; Lu, Z.; Liu, N.; Zhu, J. Challenges and Recent Progress in the Development of Si Anodes for Lithium-Ion Battery. *Adv. Energy Mater.* **2017**, *7* (23), 1700715. https://doi.org/10.1002/aenm.201700715.

(15) Peled, E.; Menkin, S. Review—SEI: Past, Present and Future. *J. Electrochem. Soc.* **2017**, *164* (7), A1703–A1719. https://doi.org/10.1149/2.1441707jes.

(16) Chu, Y.; Shen, Y.; Guo, F.; Zhao, X.; Dong, Q.; Zhang, Q.; Li, W.; Chen, H.; Luo, Z.; Chen, L. Advanced Characterizations of Solid Electrolyte Interphases in Lithium-Ion Batteries. *Electrochem. Energy Rev.* **2019**. https://doi.org/10.1007/s41918-019-00058-y.

(17) Chagnes, A.; Swiatowska, J. Electrolyte and Solid-Electrolyte Interphase Layer in Lithium-Ion Batteries. In *Lithium Ion Batteries - New Developments*; Belharouak, I., Ed.; InTech, 2012; pp 145–172. https://doi.org/10.5772/31112.

(18) Chagnes, A.; Carré, B.; Willmann, P.; Dedryvère, R.; Gonbeau, D.; Lemordant, D. Cycling Ability of γ-Butyrolactone-Ethylene Carbonate Based Electrolytes. *J. Electrochem. Soc.* **2003**, *150* (9), A1255. https://doi.org/10.1149/1.1597882.

(19) Zhang, S.; He, M.; Su, C.-C.; Zhang, Z. Advanced Electrolyte/Additive for Lithium-Ion Batteries with Silicon Anode. *Curr. Opin. Chem. Eng.* **2016**, *13*, 24–35. https://doi.org/10.1016/j.coche.2016.08.003.

(20) Xu, K.; von Cresce, A. Interfacing Electrolytes with Electrodes in Li Ion Batteries. *J. Mater. Chem.* **2011**, *21* (27), 9849. https://doi.org/10.1039/c0jm04309e.

(21) Nie, M.; Abraham, D. P.; Seo, D. M.; Chen, Y.; Bose, A.; Lucht, B. L. Role of Solution Structure in Solid Electrolyte Interphase Formation on Graphite with $LiPF_6$ in Propylene Carbonate. *J. Phys. Chem. C* **2013**, *117* (48), 25381–25389. https://doi.org/10.1021/jp409765w.

(22) Ohara, S.; Suzuki, J.; Sekine, K.; Takamura, T. Li Insertion/Extraction Reaction at a Si Film Evaporated on a Ni Foil. *J. Power Sources* **2003**, *119–121*, 591–596. https://doi.org/10.1016/S0378-7753(03)00301-X.

(23) Schroder, K. W.; Celio, H.; Webb, L. J.; Stevenson, K. J. Examining Solid Electrolyte Interphase Formation on Crystalline Silicon Electrodes: Influence of Electrochemical Preparation and Ambient Exposure Conditions. *J. Phys. Chem. C* **2012**, *116* (37), 19737–19747. https://doi.org/10.1021/jp307372m.

(24) Pereira-Nabais, C.; Światowska, J.; Chagnes, A.; Ozanam, F.; Gohier, A.; Tran-Van, P.; Cojocaru, C.-S.; Cassir, M.; Marcus, P. Interphase Chemistry of Si Electrodes Used as Anodes in Li-Ion Batteries. *Appl. Surf. Sci.* **2013**, *266*, 5–16. https://doi.org/10.1016/j.apsusc.2012.10.165.

(25) Chen, L.; Wang, K.; Xie, X.; Xie, J. Effect of Vinylene Carbonate (VC) as Electrolyte Additive on Electrochemical Performance of Si Film Anode for Lithium Ion Batteries. *J. Power Sources* **2007**, *174* (2), 538–543. https://doi.org/10.1016/j.jpowsour.2007.06.149.

(26) Dalavi, S.; Guduru, P.; Lucht, B. L. Performance Enhancing Electrolyte Additives for Lithium Ion Batteries with Silicon Anodes. *J. Electrochem. Soc.* **2012**, *159* (5), A642. https://doi.org/10.1149/2.076205jes.

(27) Ulldemolins, M.; Le Cras, F.; Pecquenard, B.; Phan, V. P.; Martin, L.; Martinez, H. Investigation on the Part Played by the Solid Electrolyte Interphase on the Electrochemical Performances of the Silicon Electrode for Lithium-Ion Batteries. *J. Power Sources* **2012**, *206*, 245–252. https://doi.org/10.1016/j.jpowsour.2012.01.095.

(28) Jaumann, T.; Balach, J.; Langklotz, U.; Sauchuk, V.; Fritsch, M.; Michaelis, A.; Teltevskij, V.; Mikhailova, D.; Oswald, S.; Klose, M.; Stephani, G.; Hauser, R.; Eckert, J.; Giebeler, L. Lifetime vs. Rate Capability: Understanding the Role of FEC and VC in High-Energy Li-Ion Batteries with Nano-Silicon Anodes. *Energy Storage Mater.* **2017**, *6*, 26–35. https://doi.org/10.1016/j.ensm.2016.08.002.

(29) Yohannes, Y. B.; Lin, S. D.; Wu, N.-L. In Situ DRIFTS Analysis of Solid Electrolyte Interphase of Si-Based Anode with and without Fluoroethylene Carbonate Additive. *J. Electrochem. Soc.* **2017**, *164* (14), A3641–A3648. https://doi.org/10.1149/2.0681714jes.

(30) Rezqita, A.; Sauer, M.; Foelske, A.; Kronberger, H.; Trifonova, A. The Effect of Electrolyte Additives on Electrochemical Performance of Silicon/Mesoporous Carbon (Si/MC) for Anode Materials for Lithium-Ion Batteries. *Electrochimica Acta* **2017**, *247*, 600–609. https://doi.org/10.1016/j.electacta.2017.06.128.

(31) Profatilova, I. A.; Stock, C.; Schmitz, A.; Passerini, S.; Winter, M. Enhanced Thermal Stability of a Lithiated Nano-Silicon Electrode by Fluoroethylene Carbonate and Vinylene Carbonate. *J. Power Sources* **2013**, *222*, 140–149. https://doi.org/10.1016/j.jpowsour.2012.08.066.

(32) Gao, H.; Xiao, L.; Plümel, I.; Xu, G.-L.; Ren, Y.; Zuo, X.; Liu, Y.; Schulz, C.; Wiggers, H.; Amine, K.; Chen, Z. Parasitic Reactions in Nanosized Silicon Anodes for Lithium-Ion Batteries. *Nano Lett.* **2017**, *17* (3), 1512–1519. https://doi.org/10.1021/acs.nanolett.6b04551.

(33) Nakai, H.; Kubota, T.; Kita, A.; Kawashima, A. Investigation of the Solid Electrolyte Interphase Formed by Fluoroethylene Carbonate on Si Electrodes. *J. Electrochem. Soc.* **2011**, *158* (7), A798. https://doi.org/10.1149/1.3589300.

(34) Schiele, A.; Breitung, B.; Hatsukade, T.; Berkes, B. B.; Hartmann, P.; Janek, J.; Brezesinski, T. The Critical Role of Fluoroethylene Carbonate in the Gassing of Silicon Anodes for Lithium-Ion Batteries. *ACS Energy Lett.* **2017**, *2* (10), 2228–2233. https://doi.org/10.1021/acsenergylett.7b00619.

(35) Jung, R.; Metzger, M.; Haering, D.; Solchenbach, S.; Marino, C.; Tsiouvaras, N.; Stinner, C.; Gasteiger, H. A. Consumption of Fluoroethylene Carbonate (FEC) on Si-C Composite Electrodes for Li-Ion Batteries. *J. Electrochem. Soc.* **2016**, *163* (8), A1705–A1716. https://doi.org/10.1149/2.0951608jes.

(36) Kim, K.; Park, I.; Ha, S.-Y.; Kim, Y.; Woo, M.-H.; Jeong, M.-H.; Shin, W. C.; Ue, M.; Hong, S. Y.; Choi, N.-S. Understanding the Thermal Instability of Fluoroethylene Carbonate in $LiPF_6$ -Based Electrolytes for Lithium Ion Batteries. *Electrochimica Acta* **2017**, *225*, 358–368. https://doi.org/10.1016/j.electacta.2016.12.126.

(37) Park, J. M.; Kim, S.; Ha, J. H.; Kim, S. W.; Lee, J.; Park, S.; Cho, B.-W.; Choi, H.-J. Enhancing the Stability of Silicon Nanosheets Electrodes by Fluoroethylene Carbonate. *Chem. Phys. Lett.* **2017**, *684*, 383–389. https://doi.org/10.1016/j.cplett.2017.07.009.

(38) Jin, Y.; Kneusels, N.-J. H.; Magusin, P. C. M. M.; Kim, G.; Castillo-Martínez, E.; Marbella, L. E.; Kerber, R. N.; Howe, D. J.; Paul, S.; Liu, T.; Grey, C. P. Identifying the Structural Basis for the Increased Stability of the Solid Electrolyte Interphase Formed on Silicon with the Additive Fluoroethylene Carbonate. *J. Am. Chem. Soc.* **2017**, *139* (42), 14992–15004. https://doi.org/10.1021/jacs.7b06834.

(39) Horowitz, Y.; Han, H.-L.; Soto, F. A.; Ralston, W. T.; Balbuena, P. B.; Somorjai, G. A.

Fluoroethylene Carbonate as a Directing Agent in Amorphous Silicon Anodes: Electrolyte Interface Structure Probed by Sum Frequency Vibrational Spectroscopy and Ab Initio Molecular Dynamics. *Nano Lett.* **2018**, *18* (2), 1145–1151. https://doi.org/10.1021/acs.nanolett.7b04688.

(40) Choi, N.-S.; Yew, K. H.; Lee, K. Y.; Sung, M.; Kim, H.; Kim, S.-S. Effect of Fluoroethylene Carbonate Additive on Interfacial Properties of Silicon Thin-Film Electrode. *J. Power Sources* **2006**, *161* (2), 1254–1259. https://doi.org/10.1016/j.jpowsour.2006.05.049.

(41) Etacheri, V.; Haik, O.; Goffer, Y.; Roberts, G. A.; Stefan, I. C.; Fasching, R.; Aurbach, D. Effect of Fluoroethylene Carbonate (FEC) on the Performance and Surface Chemistry of Si-Nanowire Li-Ion Battery Anodes. *Langmuir* **2012**, *28* (1), 965–976. https://doi.org/10.1021/la203712s.

(42) Bordes, A.; Eom, K.; Fuller, T. F. The Effect of Fluoroethylene Carbonate Additive Content on the Formation of the Solid-Electrolyte Interphase and Capacity Fade of Li-Ion Full-Cell Employing Nano Si–Graphene Composite Anodes. *J. Power Sources* **2014**, *257*, 163–169. https://doi.org/10.1016/j.jpowsour.2013.12.144.

(43) Hu, Y.-S.; Demir-Cakan, R.; Titirici, M.-M.; Müller, J.-O.; Schlögl, R.; Antonietti, M.; Maier, J. Superior Storage Performance of a Si@SiOx/C Nanocomposite as Anode Material for Lithium-Ion Batteries. *Angew. Chem. Int. Ed.* **2008**, *47* (9), 1645–1649. https://doi.org/10.1002/anie.200704287.

(44) Gong, H.; Sun, S.-G.; Li, J.-T.; Chen, Y.-J.; Chen, S.-P. Surface Combinatorial Studies of IR Properties of Nanostructured Ru Film Electrodes Using CO as Probe Molecule. *Electrochimica Acta* **2003**, *48* (20–22), 2933–2942. https://doi.org/10.1016/S0013-4686(03)00358-X.

(45) Delpuech, N.; Mazouzi, D.; Dupré, N.; Moreau, P.; Cerbelaud, M.; Bridel, J. S.; Badot, J.-C.; De Vito, E.; Guyomard, D.; Lestriez, B.; Humbert, B. Critical Role of Silicon Nanoparticles Surface on Lithium Cell Electrochemical Performance Analyzed by FTIR, Raman, EELS, XPS, NMR, and BDS Spectroscopies. *J. Phys. Chem. C* **2014**, *118* (31), 17318–17331. https://doi.org/10.1021/jp503949y.

(46) Yang, J.; Solomatin, N.; Kraytsberg, A.; Ein-Eli, Y. *In-Situ* Spectro-Electrochemical Insight Revealing Distinctive Silicon Anode Solid Electrolyte Interphase Formation in a Lithium-Ion Battery. *ChemistrySelect* **2016**, *1* (3), 572–576. https://doi.org/10.1002/slct.201600119.

(47) Dalla Corte, D. A.; Gouget-Laemmel, A. C.; Lahlil, K.; Caillon, G.; Jordy, C.; Chazalviel, J.-N.; Gacoin, T.; Rosso, M.; Ozanam, F. Molecular Grafting on Silicon Anodes: Artificial Solid-Electrolyte Interphase and Surface Stabilization. *Electrochimica Acta* **2016**, *201*, 70–77. https://doi.org/10.1016/j.electacta.2016.03.105.

(48) Koo, B. M.; Corte, D. A. D.; Chazalviel, J.-N.; Maroun, F.; Rosso, M.; Ozanam, F. Lithiation Mechanism of Methylated Amorphous Silicon Unveiled by Operando ATR-FTIR Spectroscopy. *Adv. Energy Mater.* **2018**, *8* (13), 1702568. https://doi.org/10.1002/aenm.201702568.

(49) Nguyen, C. C.; Song, S.-W. Characterization of SEI Layer Formed on High Performance Si–Cu Anode in Ionic Liquid Battery Electrolyte. *Electrochem. Commun.* **2010**, *12* (11), 1593–1595. https://doi.org/10.1016/j.elecom.2010.09.003.

(50) Li, J.-T.; Maurice, V.; Swiatowska-Mrowiecka, J.; Seyeux, A.; Zanna, S.; Klein, L.; Sun, S.-G.; Marcus, P. XPS, Time-of-Flight-SIMS and Polarization Modulation IRRAS Study of Cr2O3 Thin Film Materials as Anode for Lithium Ion Battery. *Electrochimica Acta* **2009**, *54* (14), 3700–3707. https://doi.org/10.1016/j.electacta.2009.01.052.

(51) Li, J.-T.; Swiatowska, J.; Seyeux, A.; Huang, L.; Maurice, V.; Sun, S.-G.; Marcus, P. XPS and ToF-SIMS Study of Sn–Co Alloy Thin Films as Anode for Lithium Ion Battery. *J. Power Sources* **2010**, *195* (24), 8251–8257. https://doi.org/10.1016/j.jpowsour.2010.07.043.

(52) Liao, F.; Światowska, J.; Maurice, V.; Seyeux, A.; Klein, L. H.; Zanna, S.; Marcus, P. Electrochemical Lithiation and Passivation Mechanisms of Iron Monosulfide Thin Film as Negative Electrode Material for Lithium-Ion Batteries Studied by Surface Analytical Techniques. *Appl. Surf. Sci.* **2013**, *283*, 888–899. https://doi.org/10.1016/j.apsusc.2013.07.039.

(53) Ota, H.; Sakata, Y.; Inoue, A.; Yamaguchi, S. Analysis of Vinylene Carbonate Derived SEI Layers on Graphite Anode. *J. Electrochem. Soc.* **2004**, *151* (10), A1659. https://doi.org/10.1149/1.1785795.

(54) Tian, B.; Światowska, J.; Maurice, V.; Zanna, S.; Seyeux, A.; Marcus, P. Binary Iron-Chromium Oxide as Negative Electrode for Lithium-Ion Micro-Batteries – Spectroscopic and Microscopic Characterization. *Appl. Surf. Sci.* **2015**, *353*, 1170–1178. https://doi.org/10.1016/j.apsusc.2015.07.041.

(55) Ota, H.; Akai, T.; Namita, H.; Yamaguchi, S.; Nomura, M. XAFS and TOF–SIMS Analysis of SEI Layers on Electrodes. *J. Power Sources* **2003**, *119–121*, 567–571. https://doi.org/10.1016/S0378-7753(03)00291-X.

(56) Bordes, A.; De Vito, E.; Haon, C.; Boulineau, A.; Montani, A.; Marcus, P. Multiscale Investigation of Silicon Anode Li Insertion Mechanisms by Time-of-Flight Secondary Ion Mass Spectrometer Imaging Performed on an In Situ Focused Ion Beam Cross Section. *Chem. Mater.* **2016**, *28* (5), 1566–1573. https://doi.org/10.1021/acs.chemmater.6b00155.

(57) Ling, M.; Xu, Y.; Zhao, H.; Gu, X.; Qiu, J.; Li, S.; Wu, M.; Song, X.; Yan, C.; Liu, G.; Zhang, S. Dual-Functional Gum Arabic Binder for Silicon Anodes in Lithium Ion Batteries. *Nano Energy* **2015**, *12*, 178–185. https://doi.org/10.1016/j.nanoen.2014.12.011.

(58) Liu, J.; Galpaya, D. G. D.; Yan, L.; Sun, M.; Lin, Z.; Yan, C.; Liang, C.; Zhang, S. Exploiting a Robust Biopolymer Network Binder for an Ultrahigh-Areal-Capacity Li–S Battery. *Energy Environ. Sci.* **2017**, *10* (3), 750–755. https://doi.org/10.1039/C6EE03033E.

(59) Huang, S.; Cheong, L.-Z.; Wang, S.; Wang, D.; Shen, C. In-Situ Study of Surface Structure Evolution of Silicon Anodes by Electrochemical Atomic Force Microscopy. *Appl. Surf. Sci.* **2018**, *452*, 67–74. https://doi.org/10.1016/j.apsusc.2018.05.020.

(60) Huang, S.; Cheong, L.-Z.; Wang, D.; Shen, C. Nanostructured Phosphorus Doped Silicon/Graphite Composite as Anode for High-Performance Lithium-Ion Batteries. *ACS Appl. Mater. Interfaces* **2017**, *9* (28), 23672–23678. https://doi.org/10.1021/acsami.7b04361.

(61) Harks, P. P. R. M. L.; Mulder, F. M.; Notten, P. H. L. In Situ Methods for Li-Ion Battery Research: A Review of Recent Developments. *J. Power Sources* **2015**, *288*, 92–105. https://doi.org/10.1016/j.jpowsour.2015.04.084.

(62) Hou, C.; Han, J.; Liu, P.; Yang, C.; Huang, G.; Fujita, T.; Hirata, A.; Chen, M. Operando Observations of SEI Film Evolution by Mass- Sensitive Scanning Transmission Electron Microscopy. *Adv. Energy Mater.* **2019**, *9* (45), 1902675. https://doi.org/10.1002/aenm.201902675.

(63) Tang, H.; Zhang, J.; Zhang, Y. J.; Xiong, Q. Q.; Tong, Y. Y.; Li, Y.; Wang, X. L.; Gu, C. D.; Tu, J. P. Porous Reduced Graphene Oxide Sheet Wrapped Silicon Composite Fabricated by Steam Etching for Lithium-Ion Battery Application. *J. Power Sources* **2015**, *286*, 431–437. https://doi.org/10.1016/j.jpowsour.2015.03.185.

(64) Philippe, B.; Dedryvère, R.; Allouche, J.; Lindgren, F.; Gorgoi, M.; Rensmo, H.; Gonbeau, D.; Edström, K. Nanosilicon Electrodes for Lithium-Ion Batteries: Interfacial Mechanisms Studied by Hard and Soft X-Ray Photoelectron Spectroscopy. *Chem. Mater.* **2012**, *24* (6), 1107–1115. https://doi.org/10.1021/cm2034195.

(65) Cui, L.-F.; Ruffo, R.; Chan, C. K.; Peng, H.; Cui, Y. Crystalline-Amorphous Core−Shell Silicon Nanowires for High Capacity and High Current Battery Electrodes. *Nano Lett.* **2009**, *9* (1), 491–495. https://doi.org/10.1021/nl8036323.

(66) Laïk, B.; Ung, D.; Caillard, A.; Sorin Cojocaru, C.; Pribat, D.; Pereira-Ramos, J.-P. An Electrochemical and Structural Investigation of Silicon Nanowires as Negative Electrode for Li-Ion Batteries. *J. Solid State Electrochem.* **2010**, *14* (10), 1835–1839. https://doi.org/10.1007/s10008-010-1045-5.

(67) Hou, X.; Zhang, M.; Wang, J.; Hu, S.; Liu, X.; Shao, Z. High Yield and Low-Cost Ball Milling Synthesis of Nano-Flake Si@SiO_2 with Small Crystalline Grains and Abundant Grain Boundaries as a Superior Anode for Li-Ion Batteries. *J. Alloys Compd.* **2015**, *639*, 27–35. https://doi.org/10.1016/j.jallcom.2015.03.127.

(68) Pollak, E.; Salitra, G.; Baranchugov, V.; Aurbach, D. In Situ Conductivity, Impedance Spectroscopy, and Ex Situ Raman Spectra of Amorphous Silicon during the Insertion/Extraction of Lithium. *J. Phys. Chem. C* **2007**, *111* (30), 11437–11444. https://doi.org/10.1021/jp0729563.

(69) Gauthier, M.; Danet, J.; Lestriez, B.; Roué, L.; Guyomard, D.; Moreau, P. Nanoscale Compositional Changes during First Delithiation of Si Negative Electrodes. *J. Power Sources* **2013**, *227*, 237–242. https://doi.org/10.1016/j.jpowsour.2012.11.047.

(70) Chen, L. B.; Xie, J. Y.; Yu, H. C.; Wang, T. H. An Amorphous Si Thin Film Anode with High Capacity and Long Cycling Life for Lithium Ion Batteries. *J. Appl. Electrochem.* **2009**, *39* (8), 1157–1162. https://doi.org/10.1007/s10800-008-9774-1.

(71) Baranchugov, V.; Markevich, E.; Pollak, E.; Salitra, G.; Aurbach, D. Amorphous Silicon Thin Films as a High Capacity Anodes for Li-Ion Batteries in Ionic Liquid Electrolytes. *Electrochem. Commun.* **2007**, *9* (4), 796–800. https://doi.org/10.1016/j.elecom.2006.11.014.

(72) Jeschull, F.; Lindgren, F.; Lacey, M. J.; Björefors, F.; Edström, K.; Brandell, D. Influence of Inactive Electrode Components on Degradation Phenomena in Nano-Si Electrodes for Li-Ion Batteries. *J. Power Sources* **2016**, *325*, 513–524. https://doi.org/10.1016/j.jpowsour.2016.06.059.

(73) Ermolieff, A.; Martin, F.; Amouroux, A.; Marthon, S.; Westendorp, J. F. M. Surface Composition Analysis of HF Vapour Cleaned Silicon by X-Ray Photoelectron Spectroscopy. *Appl. Surf. Sci.* **1991**, *48–49*, 178–184.

https://doi.org/10.1016/0169-4332(91)90327-G.

(74) Cardinaud, Ch.; Rhounna, A.; Turban, G.; Grolleau, B. Analyse XPS Des Surfaces de Si et SiO_2 Exposées Aux Plasmas de CHF_3 et CHF_3—C_2F_6. Polymérisation et Gravure. *Rev. Phys. Appliquée* **1989**, *24* (3), 309–321. https://doi.org/10.1051/rphysap:01989002403030900.

(75) Lehner, A.; Steinhoff, G.; Brandt, M. S.; Eickhoff, M.; Stutzmann, M. Hydrosilylation of Crystalline Silicon (111) and Hydrogenated Amorphous Silicon Surfaces: A Comparative x-Ray Photoelectron Spectroscopy Study. *J. Appl. Phys.* **2003**, *94* (4), 2289–2294. https://doi.org/10.1063/1.1593223.

(76) Gruntz, K. J.; Ley, L.; Johnson, R. L. Photoelectron Spectra of Fluorinated Amorphous Silicon (a -Si: F). *Phys. Rev. B* **1981**, *24* (4), 2069–2080. https://doi.org/10.1103/PhysRevB.24.2069.

(77) Philippe, B.; Dedryvère, R.; Gorgoi, M.; Rensmo, H.; Gonbeau, D.; Edström, K. Improved Performances of Nanosilicon Electrodes Using the Salt LiFSI: A Photoelectron Spectroscopy Study. *J. Am. Chem. Soc.* **2013**, *135* (26), 9829–9842. https://doi.org/10.1021/ja403082s.

(78) Konstadinidis, K.; Zhang, P.; Opila, R. L.; Allara, D. L. An In-Situ X-Ray Photoelectron Study of the Interaction between Vapor-Deposited Ti Atoms and Functional Groups at the Surfaces of Self-Assembled Monolayers. *Surf. Sci.* **1995**, *338* (1–3), 300–312. https://doi.org/10.1016/0039-6028(95)80048-4.

(79) Philippe, B.; Hahlin, M.; Edström, K.; Gustafsson, T.; Siegbahn, H.; Rensmo, H. Photoelectron Spectroscopy for Lithium Battery Interface Studies. *J. Electrochem. Soc.* **2015**, *163* (2), A178–A191. https://doi.org/10.1149/2.0051602jes.

(80) Etacheri, V.; Geiger, U.; Gofer, Y.; Roberts, G. A.; Stefan, I. C.; Fasching, R.; Aurbach, D. Exceptional Electrochemical Performance of Si-Nanowires in 1,3-Dioxolane Solutions: A Surface Chemical Investigation. *Langmuir* **2012**, *28* (14), 6175–6184. https://doi.org/10.1021/la300306v.

(81) Andersson, A. M.; Edström, K. Chemical Composition and Morphology of the Elevated Temperature SEI on Graphite. *J. Electrochem. Soc.* **2001**, *148* (10), A1100. https://doi.org/10.1149/1.1397771.

(82) Malmgren, S.; Ciosek, K.; Hahlin, M.; Gustafsson, T.; Gorgoi, M.; Rensmo, H.; Edström, K. Comparing Anode and Cathode Electrode/Electrolyte Interface Composition and Morphology Using Soft and Hard X-Ray Photoelectron Spectroscopy. *Electrochimica Acta* **2013**, *97*, 23–32. https://doi.org/10.1016/j.electacta.2013.03.010.

(83) Zazzera, L. A. XPS and SIMS Study of Anhydrous HF and UV/Ozone-Modified Silicon (100) Surfaces. *J. Electrochem. Soc.* **1989**, *136* (2), 484. https://doi.org/10.1149/1.2096659.

(84) Campion, C. L.; Li, W.; Lucht, B. L. Thermal Decomposition of $LiPF_6$-Based Electrolytes for Lithium-Ion Batteries. *J. Electrochem. Soc.* **2005**, *152* (12), A2327. https://doi.org/10.1149/1.2083267.

(85) Wilken, S.; Treskow, M.; Scheers, J.; Johansson, P.; Jacobsson, P. Initial Stages of Thermal Decomposition of LiPF6-Based Lithium Ion Battery Electrolytes by Detailed Raman and NMR Spectroscopy. *RSC Adv.* **2013**, *3* (37), 16359. https://doi.org/10.1039/c3ra42611d.

(86) Dupré, N.; Moreau, P.; De Vito, E.; Quazuguel, L.; Boniface, M.; Bordes, A.; Rudisch, C.; Bayle-Guillemaud, P.; Guyomard, D. Multiprobe Study of the Solid Electrolyte Interphase on Silicon-Based Electrodes in Full-Cell Configuration. *Chem. Mater.* **2016**, *28* (8), 2557–2572. https://doi.org/10.1021/acs.chemmater.5b04461.

(87) Dedryvère, R.; Gireaud, L.; Grugeon, S.; Laruelle, S.; Tarascon, J.-M.; Gonbeau, D. Characterization of Lithium Alkyl Carbonates by X-Ray Photoelectron Spectroscopy: Experimental and Theoretical Study. *J. Phys. Chem. B* **2005**, *109* (33), 15868–15875. https://doi.org/10.1021/jp051626k.

(88) Radvanyi, E.; De Vito, E.; Porcher, W.; Jouanneau Si Larbi, S. An XPS/AES Comparative Study of the Surface Behaviour of Nano-Silicon Anodes for Li-Ion Batteries. *J Anal Spectrom* **2014**, *29* (6), 1120–1131. https://doi.org/10.1039/C3JA50362C.

(89) Kang, S.-H.; Abraham, D. P.; Xiao, A.; Lucht, B. L. Investigating the Solid Electrolyte Interphase Using Binder-Free Graphite Electrodes. *J. Power Sources* **2008**, *175* (1), 526–532. https://doi.org/10.1016/j.jpowsour.2007.08.112.

(90) Zhuk, S.; Isaev, V.; Grishenkova, O.; Isakov, A.; Apisarov, A.; Zaykov, Y. Silicon Electrodeposition from Chloride-Fluoride Melts Containing K2SiF6 and SiO2. *J. Serbian Chem. Soc.* **2017**, *82* (1), 51–62. https://doi.org/10.2298/JSC160712109Z.

(91) Gaudig, M.; Naumann, V.; Hirsch, J.; Werner, M.; Großer, S.; Hagendorf, C.; Bernhard, N.; Lausch, D. Formation and Evolution of the SiOxFy Masking Layer Caused by Plasma Texturing; IEEE, 2018; pp 0036–0040.

(92) Maranchi, J. P.; Hepp, A. F.; Evans, A. G.; Nuhfer, N. T.; Kumta, P. N. Interfacial Properties of the A-Si/Cu:Active–Inactive Thin-Film Anode System for Lithium-Ion Batteries. *J. Electrochem. Soc.* **2006**, *153* (6), A1246. https://doi.org/10.1149/1.2184753.

(93) Cao, C.; Abate, I. I.; Sivonxay, E.; Shyam, B.; Jia, C.; Moritz, B.; Devereaux, T. P.; Persson, K. A.; Steinrück, H.-G.; Toney, M. F. Solid Electrolyte Interphase on Native Oxide-Terminated Silicon Anodes for Li-Ion Batteries. *Joule* **2019**, *3* (3), 762–781. https://doi.org/10.1016/j.joule.2018.12.013.

(94) Rezvani, S. J.; Nobili, F.; Gunnella, R.; Ali, M.; Tossici, R.; Passerini, S.; Di Cicco, A. SEI Dynamics in Metal Oxide Conversion Electrodes of Li-Ion Batteries. *J. Phys. Chem. C* **2017**, *121* (47), 26379–26388. https://doi.org/10.1021/acs.jpcc.7b08259.

(95) Li, J.-T.; Światowska, J.; Maurice, V.; Seyeux, A.; Huang, L.; Sun, S.-G.; Marcus, P. XPS and ToF-SIMS Study of Electrode Processes on Sn−Ni Alloy Anodes for Li-Ion Batteries. *J. Phys. Chem. C* **2011**, *115* (14), 7012–7018. https://doi.org/10.1021/jp201232n.

(96) Morita, M.; Asai, Y.; Yoshimoto, N.; Ishikawa, M. A Raman Spectroscopic Study of Organic Electrolyte Solutions Based on Binary Solvent Systems of Ethylene Carbonate with Low Viscosity Solvents Which Dissolve Different Lithium Salts. *J. Chem. Soc. Faraday Trans.* **1998**, *94* (23), 3451–3456. https://doi.org/10.1039/a806278a.

(97) Fukushima, T.; Matsuda, Y.; Hashimoto, H.; Arakawa, R. Studies on Solvation of Lithium Ions in Organic Electrolyte Solutions by Electrospray Ionization-Mass Spectroscopy. *Electrochem. Solid-State Lett.* **2001**, *4* (8), A127. https://doi.org/10.1149/1.1383428.

(98) Masia, M.; Probst, M.; Rey, R. Ethylene Carbonate−Li^+: A Theoretical Study of Structural and Vibrational Properties in Gas and Liquid Phases. *J. Phys. Chem. B* **2004**, *108* (6), 2016–2027. https://doi.org/10.1021/jp036673w.

(99) Wang, Y.; Balbuena, P. B. Theoretical Studies on Cosolvation of Li Ion and Solvent

Reductive Decomposition in Binary Mixtures of Aliphatic Carbonates. *Int. J. Quantum Chem.* **2005**, *102* (5), 724–733. https://doi.org/10.1002/qua.20466.

(100) Ikezawa, Y.; Ariga, T. In Situ FTIR Spectra at the Cu Electrode/Propylene Carbonate Solution Interface. *Electrochimica Acta* **2007**, *52* (7), 2710–2715. https://doi.org/10.1016/j.electacta.2006.09.050.

(101) Joho, F.; Novák, P. SNIFTIRS Investigation of the Oxidative Decomposition of Organic-Carbonate-Based Electrolytes for Lithium-Ion Cells. *Electrochimica Acta* **2000**, *45* (21), 3589–3599. https://doi.org/10.1016/S0013-4686(00)00480-1.

(102) Aurbach, D. A Comparative Study of Synthetic Graphite and Li Electrodes in Electrolyte Solutions Based on Ethylene Carbonate-Dimethyl Carbonate Mixtures. *J. Electrochem. Soc.* **1996**, *143* (12), 3809. https://doi.org/10.1149/1.1837300.